Complex geomorphologic assemblage of terrains in association with the banded terrain in Hellas basin, Mars

X. Diot[1, 2], M.R. El-Maarry[3], F. Schlunegger[1], K.P. Norton[4], N. Thomas[2, 3], P.M. Grindrod[5,6] and M. Chojnacki[7]

[1]Institut für Geologie Universität Bern, Baltzerstrasse 1-3 CH-3012 Berne, Switzerland.

[2]Center for Space and Habitability, Universität Bern, Sidlerstrasse 5 CH- 3012 Berne, Switzerland.

[3]Physikalisches Institut, Universität Bern, Sidlerstrasse 5 CH- 3012 Berne, Switzerland.

[4]School for Geography, Environment and Earth Science, Victoria University of Wellington, New Zealand.

[5]Department of Earth and Planetary Sciences, Birkbeck, University of London, London, UK

[6]Centre for Planetary Sciences at UCL/Birkbeck, London, UK.

[7]Lunar and Planetary Laboratory, University of Arizona, Tucson, AZ 85721, United States

Corresponding author

Xavier Diot

Institut für Geologie Universität Bern

Baltzerstrasse 1-3 CH-3012, Switzerland

E-mail address: xavier.diot@csh.unibe.ch

Number of Tables: 2

Number of Figures: 16

Submitted to Planetary & Space Science

Highlights

- Hellas basin's NW interior displays a complex assemblage of terrains.
- The banded terrain may be the youngest widespread domain of Hellas.
- The banded terrain may have covered a large part of the NW interior of Hellas.
- The geologic activity seems to have significantly dwindled in the Amazonian.

Abstract

Hellas basin acts as a major sink for the southern highlands of Mars and is likely to have recorded several episodes of sedimentation and erosion**.** The north-western part of the basin displays a potentially unique Amazonian landscape domain in the deepest part of Hellas, called “banded terrain”, which is a deposit characterized by an alternation of narrow band shapes and inter-bands displaying a sinuous and relatively smooth surface texture suggesting a viscous flow origin. Here we use high-resolution (HiRISE and CTX) images to assess the geomorphological interaction of the banded terrain with the surrounding geomorphologic domains in the NW interior of Hellas to gain a better understanding of the geological evolution of the region as a whole. Our analysis reveals that the banded terrain is associated with six geomorphologic domains: a central plateau named Alpheus Colles, plain deposits (P1 and P2), reticulate (RT1 and RT2) and honeycomb terrains. Based on the analysis of the geomorphology of these domains and their cross-cutting relationships, we show that no widespread deposition post-dates the formation of the banded terrain, which implies that this domain is the youngest and latest deposit of the interior of Hellas. Therefore, the level of geologic activity in the NW Hellas during the Amazonian appears to have been relatively low and restricted to modification of the landscape through mechanical weathering, aeolian and periglacial processes. Thermophysical data and cross-cutting relationships support hypotheses of modification of the honeycomb terrain via vertical rise of diapirs such as ice diapirism, and the formation of the plain deposits through deposition and remobilization of an ice-rich mantle deposit. Finally, the observed gradual transition between honeycomb and banded terrain suggests that the banded terrain may have covered a larger area of the NW interior of Hellas in the past than previously thought. This has implications on the understanding of the evolution of the deepest part of Hellas.

Keywords: Mars, surface; Geomorphological processes; Hellas basin

1. Introduction

A large part of the geological and hydrological history of Mars is preserved in the Noachian highlands that cover approximately half of the planet (Wilson et al., 2010). In its southern regions, widespread valley and channel networks are observed (e.g. Carr and Chuang, 1997; Forsythe and Blackwelder, 1998; Cabrol and Grin, 2001; Howard et al., 2005; Ansan et al., 2008). Some of these valleys terminate in craters and basins (Maxwell and Craddock, 1995; Howard et al., 2005) in the form of fans or alluvial deposits (Wilson et al., 2012). Also in this area, several ancient craters display putative shorelines and light-toned layered interior deposits that suggest that they may have harbored paleolakes (De Hon, 1992; Wilson et al., 2007; Cabrol and Grin, 2010; Ansan et al., 2011). Thus, erosional and sediment transport processes had a significant impact on the geomorphic and stratigraphic development of the southern highlands, particularly in association with impact craters, where multiple sedimentary successions have been documented.

In addition to the geomorphic evidence for fluvial deposits and erosion at the southern highlands' surface in ancient times, numerous hydrous minerals such as hydrated-silica, phyllosilicates and secondary minerals including chlorides have been detected spectrally in the southern highlands (e.g. Osterloo et al., 2008, 2010; Carter et al., 2013; Ehlmann et al., 2011, 2014). The formation of these minerals, which usually requires significant volumes of liquid water, combined with the occurrence of large drainage network systems suggests that hydrologic processes have widely shaped the landscape of Mars (Carr and Chuang, 1997; Crown et al., 2005; Matsubara et al., 2013, El-Maarry et al., 2014), especially in terrains surrounding Hellas basin (Wilson et al., 2007; Ansan et al., 2011; Ehlmann et al., 2014).

Due to its size, Hellas basin represents a major sink for the surrounding drainage network systems (e.g. Carr, 1995; Mest et al., 2001; Crown et al., 2005; Wilson et al., 2010; De Blasio, 2014) and could thus have recorded several episodes of sedimentation and erosion through volcanic, fluvial, glacial and aeolian processes (e.g. Moore and Edgett, 1993; Tanaka and Leonard, 1995; Leonard and Tanaka, 2001; Wilson et al., 2010; Bernhardt et al., 2015). Despite substantial constraints on observing Hellas basin caused by the high atmospheric aerosol content, the region has been a regular target for observation by most Mars orbiting missions (e.g. Simpson et al., 1979; Moore and Edgett; 1993; Martin and Richardson, 1993; Edwards et al., 2001; Krause and Grosfils, 2001; Smith et al., 1999, 2001; Kostama et al., 2001; Albee, 2002; Ormö and Komatsu, 2003; Plaut, 2003; Encrenaz et al., 2006; Graf et al., 2005; Grassi et al., 2007; McEwen et al., 2002, 2007 and 2010; Malin et al., 2007; Murchie et al., 2007). Studies that are based on Viking Orbiter Infrared Thermal Mapper (IRTM) data suggested that the ground of the basin is made up of indurated fine-grained material, especially in its lowest part where outcrops of bedrock are considered to be absent (Moore and Edgett, 1993). Using Viking images, Tanaka and Leonard (1995) studied the geologic and geomorphic architecture of the basin and proposed that Hellas was mainly filled by volcanic flows, which were subsequently modified by fluvial and aeolian processes. Alternatively, geomorphic studies suggested that the surface material in the interior part of Hellas was most likely formed by aqueous and glacial processes (Kargel and Strom, 1991; Wilson et al., 2010). Based on high-resolution images from the Mars Orbiter Camera (MOC), Moore and Wilhelms (2001) observed bright layered deposits along several contours and a series of polygonal depressions referred to as honeycomb material. These authors have speculated that this morphology could reflect imprints of falling ice-blocks on the non-consolidated mud at the surface. Recently, Diot et al. (2014) described a possibly unique terrain type referred to as “banded terrain” (Figs. 1A and 2). The banded terrain displays an

105 alternation of narrow bands and inter-bands where the sinuous morphology was attributed to
106 viscous flow behavior. This terrain is localized in the northwestern interior of Hellas, mainly
107 in the deepest part of the basin. Mapping and morphometric analysis (Diot et al., 2014)
108 reveals that the shape of the bands varies from linear to concentric geometries (Fig. 2).
109 However, while potential mechanisms of material transfer recorded by the banded terrain has
110 been elaborated in our previous paper (Diot et al., 2014), the stratigraphic relationship to the
111 neighboring domains has not yet been elaborated upon, which is the scope of this paper. In
112 doing so, we aim to understand better the geomorphic evolution of the deepest region of
113 Hellas within a larger temporal and spatial context.

114 Here, we investigate the geomorphological assemblage of terrains situated in the northwest
115 interior of Hellas in association with the banded terrain. This is accomplished through a
116 possible reconstruction of the history of erosion, deposition and material transport, which is
117 recorded by the landscape of Hellas. We use both newly-acquired and currently available
118 datasets to determine the cross-cutting relationships between the geomorphic domains in the
119 northwest interior of Hellas basin paying close attention to the contacts between the banded
120 terrain and neighboring domains. In section 2, we describe the geological setting. In section
121 3, we provide information on the data sets used and in section 4 we present our observations
122 and interpretations. Finally in section 5, we discuss the evolution of the northwest interior of
123 Hellas from the interpretations of our observations and the possible formation mechanism of
124 the investigated domains.

125

126 **2. Geological setting**

127 Hellas basin (centered at 40°S, 68°E) was formed through a giant oblique impact ~4 Ga ago
128 (Leonard and Tanaka, 1993; Tanaka and Leonard, 1995; Werner et al., 2008). The basin is

~2,300 km-long, ~1,500 km-wide and more than 7 km-deep with respect to the elevation reference datum (Smith et al., 1999) making it the deepest and one of the largest depressions on Mars. Consequently, it has been a major trap for sedimentary deposits and for eroded material from the surrounding highlands (e.g. Tanaka and Leonard, 1995; Moore and Wilhelms, 2001; Crown et al., 2005; Bandfield, 2008; Wilson et al., 2010).

In the northern part of the basin, sediments appear to have been supplied through a wide network of channels (Wilson et al., 2010) as indicated by the presence of fan deposits (Moore and Howard, 2005; Wilson et al., 2010). These observations have been invoked by a number of studies as evidence for a large paleo-lake within Hellas (e.g., Cabrol and Grin, 2010; Haberle et al., 2001; Moore and Wilhelms, 2001). Most of the channels probably date to the Noachian–Hesperian boundary (Fassett and Head, 2008; Wilson et al., 2010). Layered deposits of a possible subaqueous origin (Ansan et al., 2011) and hydrated minerals such as phyllosilicates and hydrated silica have been identified in Noachian-aged craters located north of Hellas (e.g., Malin and Edgett, 2000; Mest and Crown, 2005; Bandfield et al., 2008, 2013a; Crown et al., 2010; Wilson et al., 2010; Ansan et al., 2011; Fortezzo and Skinner, 2013; Chuang et al., 2015).

Geomorphic studies of the eastern part of Hellas reveal the presence of fine-grained-layered material at the eastern boundary of a large volatile-rich depositional shelf, and the occurrence of multiple channels that extend toward the basin similarly suggesting a deposition within a paleo-lake (Crown et al., 2005; Bleamaster and Crown, 2010). These observations point to a complex history of erosion and deposition in an aqueous environment during the Late Noachian- Early Hesperian (e.g. Malin and Edgett, 2000; Moore and Wilhelms, 2001; Mest and Crown, 2006; Mest et al., 2010; Wilson et al., 2010).

152 The northern and eastern flanks of the basin host multiple viscous flow features. These
153 features include small and young (Late Amazonian) ice-rich flow lobes located on slopes
154 (e.g. Milliken et al., 2003; Berman et al., 2009; Head et al., 2005; Hubbard et al., 2011), and
155 larger, and older (Early Amazonian), lobate debris aprons surrounding mounds, which were
156 interpreted to be analogous to terrestrial debris-covered glaciers (e.g. Squyres, 1979;
157 Mangold and Allemand, 2001; Mangold, 2003; Pierce and Crown, 2003; Berman et al., 2009
158 and 2015).

159 With regard to the NW interior of Hellas, which is our main study region, recent geologic
160 maps (e.g. Moore and Wilhelms, 2001) display four major domains: (i) a western band
161 referred to as the reticulate terrain, (ii) a central plateau named the Alpheus Colles (ACP),
162 (iii) widespread plains material surrounding the plateau, and (iv) honeycomb terrain.
163 According to Moore and Wilhelms (2001), the geological and geomorphic evolution of the
164 region is as follows (from the oldest to the youngest): the formation of the ACP dated to the
165 Lower Hesperian via crater counting (Tanaka and Leonard, 1995; Leonard and Tanaka,
166 2001), the reticulate terrain, the plains material where the emplacement has been dated to
167 Middle to Late Hesperian (Leonard and Tanaka, 2001), and finally the formation of the
168 honeycomb terrain. More recently, high-resolution data allowed the mapping (Figs. 1A) of an
169 additional geomorphologic domain dubbed “banded terrain” (Diot et al., 2014).

170 CTX and HiRISE images (see section 3 datasets and methods) reveal that the NW interior of
171 Hellas is largely covered by the banded terrain (Fig. 1A; Diot et al., 2014). This domain has
172 been dated to the Amazonian and displays a sinuous and smooth surface texture, suggesting
173 that the material has been displaced by a viscous flow. The domain consists of juxtapositions
174 of bands (3–15 km-long, ~0.3 km-wide) separated by narrow inter-bands depressions (~65 m-
175 wide and at least 10 m-deep). The surfaces of the bands display features such as fractured
176 mounds, polygons and sublimation landforms (e.g. progressive blocky degradation), which

may have formed in a periglacial environment (Diot et al., 2014). The banded terrain is in contact with two main domains of Hellas: the ACP to the south and the honeycomb terrain to the north (Fig. 1A). Overall, the banded terrain is present in a trough close to the NW edge of the ACP and in local places on the plateau (Fig. 1A).

3. Datasets and methods

The geomorphological investigation was carried out using: (i) the datasets from the Mars Orbiter Laser Altimeter (MOLA; Smith et al, 2001) onboard the Mars Global Surveyor, (ii) the Thermal Emission Imaging System camera (THEMIS; Christensen et al., 1999 and 2004; Edwards et al., 2011) on Mars Odyssey spacecraft, (iii) the Context Camera (CTX; Malin et al, 2007), and (iv) the High Resolution Imaging Science Experiment (HiRISE; McEwen et al., 2007), which are both onboard on the NASA's Mars Reconnaissance Orbiter. MOLA (468 m/pixel in resolution) provides an elevation map in a simple cylindrical projection of the near-entire surface of Mars. This map, combined with the THEMIS daytime infrared map (100 m/pixel in resolution) in the GIS environment JMARS (http://jmars.asu.edu; Gorelick et al., 2003), was used as a background for mapping. CTX typically obtains 30 km-wide and 40 km-long images with a resolution of ~6 m/pixel**.** We used this dataset to trace the spatial extent of the different domains, and to characterize the surface texture of the different domains and their geometric relationships. The HiRISE camera has a lower spatial coverage yet offers a high spatial resolution of 25–50 cm/pixel, which we used for detailed investigations of cross-cutting relationships at the domain boundaries, and small-scale morphologic features thereof.

The geomorphological map of the NW of Hellas (Fig. 1A) was produced using JMARS. The identification of the domains relied mainly on their textures (rough, hummocky, smooth etc.)

observed on high-resolution CTX and HiRISE images and their relative elevation on the THEMIS day-time underlying a MOLA colors map (where colors denote different elevation ranges). We thus used color differences between domains to delineate the boundaries separating them. The boundaries of the different domains were drafted using colored polylines of connected sequences of points.

We also created a 2 m/pixel HiRISE stereo Digital Terrain Model (DTM) built from the HiRISE image pair ESP_024936_1435 and ESP_033494_1435, using the commercial software SOCET SET from BAE Systems and the freely-available software Integrated Software for Imagers and Spectrometer (ISIS) from the United States Geological Survey (USGS), and utilizing previous methods (Kirk et al., 2008). Our HiRISE DTM was produced with vertical control relative to MOLA elevations. Using previous estimates (Kirk et al., 2003 and 2008), we determined a vertical accuracy of 0.271 m. This DTM was used to generate the slope and relief maps of the reticulate terrain 2 presented in the section 4.3 within the GIS environment ArcGIS 10.1. ArcGIS (http://www.esri.com/software/arcgis) allows the combination of multiple datasets including elevation, slope patterns, volumes, relief, aspect ratios, etc. We identified the relief as the elevation difference between the highest point (representing the surface of the ridges) and the lowest point (representing the bottom of the depressions; Ahnert, 1984) within 400 m × 400 m roving windows (Grohmann and Riccomini, 2009), which move horizontally on the HiRISE DTM. We have chosen a 400 m × 400 m-sized roving window because the polygonal structures of the reticulate terrain 2 (section 4.3) are approximately within this size range, which can help to gain insight on the geometry and mechanism of formation of this domain.

Finally, we derived thermal inertia maps (~100 m/pixel) from THEMIS predawn band 9 (12.57 µm) brightness temperature images using the thermal model of Putzig and Mellon (2007) and implemented in the "jENVI" software suite

(http://arsia.gg.utk.edu/~utmars/jenvi/) (see Chojnacki et al. (2014) for a more detailed description of our methodology). Thermal inertia is a key surface property controlling diurnal and seasonal temperature variations and yields insight into the physical properties (e.g., grain size, degree of induration) of the martian near-surface (Putzig and Mellon, 2007). Although thermal inertia is largely controlled by particle size, it is also influenced by other factors (e.g., degree of induration, reduced pore space) (Mellon et al., 2000; Fergason et al., 2006b; Putzig and Mellon, 2007; Piqueux and Christensen, 2009), thus making interpretations of values generally non-unique (e.g. Christensen, 1986). This ambiguity is particularly the case for regions with high concentrations of dust on the surface, which is occasionally the case in Hellas Basin. To partially mitigate this issue, we preferentially selected THEMIS data of banded terrain locations with low dust coverage as estimated by the dust cover index from thermal emission spectroscopy (Ruff and Christensen, 2002). The thermal inertia values obtained during this study are shown in Table 1.

4. Observations and Interpretations

In this section, we built up on previous (e.g. Tanaka and Leonard, 1995; Moore and Wilhelms, 2001; Bernhardt et al., 2015) descriptions of the different domains including the Alpheus Colles Plateau (ACP), plain deposits, reticulate and honeycomb terrains emphasizing their textures (rough, hummocky, smooth etc.) and their fine-scale morphology, which we have discerned using the new datasets (e.g., HiRISE). We also characterize the contacts between the domains and the recently identified banded terrain (Diot et al., 2014). Fig. 1C shows the location of the figures presented in the following sections and sub-sections.

4.1. The banded terrain

The banded terrain is characterized by a common morphology consisting of an alternation of sinuous bands and inter-bands displaying a variety of shapes including linear, concentric and lobate bands (Fig. 2). Finer-scale observations carried out using HiRISE images reveal the presence of multiple boulders on the surface of the bands (Fig. 3). These boulders have diameters in the range of 1 to 8 m, and they are clustered in multiple places (Fig. 3A). Furthermore, fresh impact craters are surrounded by halos of similar boulders more or less symmetric around the craters (Fig. 3B). Where the halo displays an asymmetric shape, the number density and the size of the boulders decrease away from the crater (Fig. 3B). In addition, multiple rockfall deposits initiating from the bands' boundaries are observed in the banded terrain (Fig. 4). The size of the falling blocks ranges between 1 and 10 m.

Another notable feature is located in the western part of the banded terrain area where we observe a tongue-shaped pattern ~3 km-long and ~0.5 km-wide (Fig. 5), which resembles features related to viscous flow features (VFFs, Milliken, et al., 2003; Souness et al., 2012; Hubbard et al., 2014). This tongue-shaped surface pattern is located ~40°S, which falls within the range of latitudes (30°–60° in both hemisphere) of VFFs (e.g. Milliken et al., 2003; Souness et al., 2012), yet is located at an elevation of -6620 m, which is much lower than the mean elevation (+885 m) of the analogous structures (Souness et al., 2012). The average MOLA slope of this feature is approximately 2° trending southward. This poleward aspect is consistent with observations made for the VFFs (e.g. Milliken et al., 2003; Berman et al., 2009; Souness et al., 2012). The morphology of this feature (Fig. 5) is consistent with that of VFFs as defined by Souness et al. (2012). Namely, (i) it has a smoother surface than the surrounding landscape (Fig. 5A); (ii) it displays stripes or lineations on the lateral margins as well as frontal ridges indicative of a down-slope flow (Figs. 5A and C); (iii) it has a length to

273 width ratio > 1; and (iv) it has a discernable closed terminus and an evasive head (Figs. 5A
274 and 5C). In addition, polygonal fractures located at the termination and multiple boulders at
275 the evasive head are well visible (Figs. 5B and D) and similar to those observed on the
276 surfaces of VFFs (e.g. Milliken et al., 2003; Hubbard et al., 2014).

277 The thermal inertia of the banded terrain (Table 1) ranges between 300 and 450 $Jm^{-2}K^{-1}s^{-1/2}$
278 (hereafter referred to as thermal inertia units [tiu]). The bands typically have higher values
279 (around 400–450 tiu), while the thermal inertia in the lower-lying inter-bands varies between
280 300 and 380 tiu. These lower values most likely reflect the presence of fine- to coarse-grained
281 sediment consistent with the aeolian mega-ripples within the inter-bands as visible in HiRISE
282 images (Fig. 6A). Additionally, we attribute part of depressed thermal inertia values detected
283 in the inter-bands to an enhanced surface dust, possibly caused by the >10 m-high elevation
284 difference between the bands and inter-bands (Diot et al., 2014). Although low, the range
285 (300–450 tiu) of thermal inertia of the banded terrain is significantly higher than that of dust
286 (<120 tiu), which indicates a relatively consolidated or cemented surface with a partial
287 coating of fine dust.

288 The elevation of the initiation points of the bands varies between -7.4 km and -5.6 km
289 (average ~-6 km). Locally, we observe a detachment of the bands from the NW boundary of
290 the central ACP (Fig. 6B). These structures may have played a significant role in the shaping
291 of the NW ACP's margin. Diot et al. (2014) interpreted the NW edge of the ACP as an
292 erosive boundary. In addition, multiple bands are located on the top of the ACP. Therefore,
293 we anticipate that the banded terrain formed after the emplacement of the ACP and that the
294 motion of the material resulted in the erosion of the NW part of the plateau.

295 North of the banded terrain lies the honeycomb terrain, which consists of a set of geomorphic
296 cells organized in a polygonal pattern (e.g. Moore and Wilhelms, 2001). The contact between

these two geomorphologic domains appears to be complex and at times ambiguous. Close to, or in contact with the banded terrain, the interior of the cells displays infills that appear morphologically similar to that of the banded terrain, in particular the linear bands (Fig. 7A1). Thus, we conclude that the banded terrain deposits overlap the honeycomb cells and thereby post-date the formation of the honeycomb terrain. Further details concerning the geometric relationships between the banded and honeycomb terrains are provided in section 4.5.

4.2. The Alpheus Colles plateau (ACP)

The ACP (Fig. 1A) is a large (~750,000 km^2) domain situated almost at the center of Hellas basin in an elevation range of -7 km to -6.2 km with an average of ~ -6.5 km. Moore and Wilhelms (2001) described this domain as a thick multilayered deposit characterized by knobs and hummocks. In CTX images, the ACP appears to be composed of a belt of chaotic terrain in the NW part (Fig. 8A) and a relatively smoother central part (Fig. 8B). The chaotic part is made up of multiple, relatively large partially elongated knobs or hills (Fig. 8A). These knobs consist of a stack of multiple dark and sometimes white layers (see white arrows and sketch in Fig. 8A). These observations are consistent with the ones by Moore and Wilhelms (2001) who recognized multiple layers on Viking images. The surface texture of the central part hosts multiple smooth lobate shapes (Fig. 8B) that drape over the floor of the ACP. We interpret this texture to have formed through a remobilization of an ice-rich mantle that was originally deposited during periods of high obliquity. In the same area, Bernhardt et al. (2015) mapped a layer of ice-rich mantle material on the top of the ACP. Moreover, the texture and shape of the lobate features (Fig. 8B) is analogous to lobate debris aprons, which

320 have also been considered to have an ice-related origin (e.g. Mangold and Allemand, 2001;
321 Pierce and Crown, 2003; Berman et al., 2015).

322 Thermal inertia data (Table 1) reveal low values (~220 tiu) for the ACP pointing to the
323 presence of a fine-grained surface material such as silt or fine sand, but not dust (<60 µm)
324 (Putzig and Mellon, 2007). Such values of thermal inertia are similar to the lowest values (4–
325 6 10^{-3}cal cm^{-2} $s^{-1/2}$/K, equivalent to 168–250 tiu) obtained by Moore and Edgett (1993) for
326 central Hellas using (IRTM), and similarly interpreted by them to represent fine sands.

327 The occurrence of large degraded and/or buried craters (Moore and Wilhelms, 2001)
328 indicates that the plateau has experienced a long erosional history and is considered to be the
329 oldest (Lower Hesperian) domain in the basin's interior (Tanaka and Leonard, 1995; Leonard
330 and Tanaka, 2001; Moore and Wilhelms, 2001; Bernhardt et al., 2015).

331

332 ***4.3. The plain deposits***

333 The northwestern interior part of the basin is covered by a widespread (~142,000 km^2)
334 material with a wavy-looking surface texture (at THEMIS images scale), situated at an
335 elevation range of -7.2 km to -6.6 km (average~ -7 km). This domain has been identified as
336 plains-forming material in previous studies (e.g. Tanaka and Leonard, 1995; Leonard and
337 Tanaka, 2001; and Moore and Wilhelms, 2007; Bernhardt et al., 2015). Two different
338 geomorphologic domains of plain deposits can be distinguished on the THEMIS day-time
339 imagery with MOLA colors map (Fig. 1A): a ~124,000 km^2-wide "plain deposit 1" domain
340 (P1, represented by a gray-violet color indicative of an elevation of ~ -6.940 km in Fig. 1A),
341 which is embayed by a smaller ~18,000 km^2-wide "plain deposit 2" domain (P2, represented
342 by a dark violet color indicative of a lower elevation of ~ -6.970 km). A slight difference in

thermal inertia (Table 1) is observed between P1 (200–260 tiu) and P2 (260–300 tiu). Such values of thermal inertia suggest the presence of a fine- grained material for P1 and P2 as silt or fine sand, similar to the ACP (Putzig and Mellon, 2007). At the scale of the THEMIS day-time data with MOLA colors map, the P1 and P2 domains show a relatively smooth and wavy featureless surface (Fig. 1A). CTX images show that the P1 domain is characterized by the presence of local round-shaped knobs whereas P2 displays a widespread and relatively smooth surface (Figs. 9 and 10A1). Accordingly, the surface of P1 appears to be more degraded than that of P2. However, using HiRISE images, the surface of P2 appears to be pitted (Figs. 10B, 10C and 11). The pits are 1–8 m-wide and have an angular shape. An uneven and sinuous morphological transition (Figs. 9A1 and A2) between P1 and P2 is clearly observable on CTX images. Along this contact (contact underlined by white arrows on Figs. 9A1, 9A2 and 9B), the shadow derived from the boundary of P2 is observed on P1, suggesting that P2 overlies P1. Moreover, we observe that a smooth material analogous to P1 seems to overlap the ACP in the eastern part of Hellas. This observation is consistent with the identification by Moore and Whilelms (2001) of a plain forming material overlapping the central plateau in the eastern interior of Hellas (Fig. S1 in the supplementary material). Moreover, the geomorphologic mapping (Fig. 1A) and geometric relationships show that P2 is in contact with the reticulate and honeycomb terrains. Indeed, P2 appears to be intermixed with some structures of the honeycomb and reticulate terrains. The details of the geometric relationships between P2 and these two domains are presented in the following sections.

4.4. The reticulate terrain

Earlier and recent studies (e.g. Moore and Wilhelms, 2001 and 2007; Wilson et al., 2010; Bernhardt et al., 2015) of the western interior of Hellas have mapped one curved band of

367 reticulate terrain named here RT1 (Figs. 1A, 10A1 and 10A2), which consists of ridges
368 organized in a polygonal pattern and separated by flat depressions that host small sinuous
369 ridges in some places. Based on the cross-cutting relationships, the size and the surface
370 texture, we identified and mapped multiple outcrops of a second geomorphologic domain of
371 reticulate terrain (RT2), situated in the northwest interior of Hellas (Figs. 1A, 10B, 10C, 11,
372 12 and 13). Similarly to RT1, the RT2 domain can be characterized by the occurrence of
373 ridges that are interconnected in a polygonal pattern and separated by relatively flat
374 depressions (Figs. 10B, 10C, 11, 12 and 13). However, the RT2 domain differs from RT1 in
375 terms of elevation and size-scale. RT1 depressions (Figs. 10A1 and 10A2), located at
376 elevations ranging from -5.9 km to -5.6 km, are larger (1–2 km across) than RT2 depressions
377 (Figs. 10B, 10C, 11, 12 and 13), which in turn are located at a lower elevation of ~-7.2 km
378 and have cross-sectional widths that range between 250 m and 1 km. Similarly, the RT1
379 ridges are larger (200 m to 1 km) than the RT2 ones, which fall in the range of ~20–100 m. In
380 addition, the HiRISE images reveal that while RT1 and RT2 ridges show a pitted surface with
381 angular boulders ~2 m in diameter, the floor of the depressions is flat and relatively smooth
382 (Figs. 10A1, 10B and 10C, 11). In one location, a network of faults oriented NW-SE is
383 observed (Figs. 10B and 10C). The faults are between 65 m and 730 m long (with an average
384 of ~230 m), and the spacing between them is irregular. The presence of triangular
385 morphologies on the top suggests a vertical offset up to the NE.

386 We used a HiRISE DTM to compute the slope and the relief of the RT2 domain (Figs. 12 and
387 13). The average slope near the ridges ranges between 30° and 50°, while the floors of the
388 depressions are ≤ 2° (Fig. 12B). Furthermore, relief profiles (profiles A–A' and B–B' on Fig.
389 13) show that the depressions between the ridges are associated with peaks of relief that
390 range between 15 and 20 m (Fig. 13). Unfortunately, a similar analysis for the RT1 domain is
391 not possible due to the lack of a similar DTM.

392 In addition to the morphometric differences, the cross-cutting relationships are also different
393 for RT1 and RT2. Indeed, in the western part of Hellas, P1 overlies the RT1 domain (Moore
394 and Wilhelms, 2001; Figs. 10A1 and 10A2). Therefore P1, and, by extension, P2 appear to
395 post-date the formation of RT1. In the northwest Hellas interior, the multiple patches of the
396 RT2 domain suggest that RT2 might have exhibited a larger spatial coverage in the past.
397 Moreover, HiRISE images show the same P2's pitted surface with boulders 1–8 m wide
398 grading into the ridges of the RT2 (Figs. 10B, 10C, 11A, 11B and 11C). Unlike RT1, the RT2
399 domain is not overlain by P1.

400

401 ***4.5. The honeycomb terrain***

402 The honeycomb terrain is extensive in the NW interior of Hellas (Fig. 1A) and located in a
403 range of elevation between -7.4 km and -7 km (average ~ -7.2 km). Moore and Wilhelms
404 (2001) named this domain in their map "honeycomb material" and described it as a belt
405 circumferential to the ACP of elliptical and polygonal rimmed shapes analogous to
406 "biological cells" (Figs. 7A1, 7A2, 14A and 14B1). These shapes have diameters 3–15 km
407 wide (e.g. Leonard and Tanaka, 2001; Moore and Wilhelms, 2001 and 2007; Wilson et al.,
408 2010) and display an overall E-W orientation. CTX images reveal that the shape of the
409 honeycomb "cells" varies from relatively concentric to elongated (Figs. 7A1 and 7B) without
410 a distinct pattern. Possible layer-like structures can be observed in some cells (see white
411 arrows on Fig. 7A2). Thermal inertia data (Table 1) reveal values of 250–350 tiu with peaks
412 around 400 tiu for the rims of the "cells", which are consistent with the values reported in
413 Moore and Edgett (1993) for the center of Hellas. This relatively low range of values is
414 indicative of a cemented sand-sized material (e.g. Putzig and Mellon, 2007). The slight

415 difference in thermal inertia between the interior and the rim of the cells is explained by the
416 preferential accumulation of fine to coarse grained material in topographic depressions.

417 The honeycomb terrain appears to be enclosed by the P2 geomorphologic domain (Fig. 14A).
418 Indeed, using CTX images, we observe that some areas of P2 form the edges of the
419 honeycomb cells. Likewise, ridges of the RT2 domain are twisted and curved in contact with
420 honeycomb cells (Fig. 14). We identified P2 and RT2 to be ubiquitous in the entire NW
421 interior region of Hellas below the honeycomb terrain (Fig. 14). In addition, HiRISE and
422 CTX images reveal that some honeycomb structures display similar surface textures to the
423 linear bands of the banded terrain (Fig. 7A1), while other cells have a relatively smooth to
424 knobby surface where they are farther away from the banded terrain (Fig. 7B).

425

426 **5. Discussion**

427 The combination of previous studies (e.g. Tanaka and Leonard, 1995; Moore and Wilhelms,
428 2001 and 2007; Wilson et al., 2010; Bernhardt et al., 2015) with our new observations of the
429 assemblage of terrains in association with the banded terrain enables us to gain an improved
430 understanding of the geologic history of the NW interior of Hellas. In the following sections,
431 we discuss the complex cross-cutting relationships of the terrains, and propose possible
432 origins for the different geomorphologic domains.

433

434 ***5.1. Evolution of the northwestern interior of Hellas***

435 The relative correlation (Fig. 15) of the different geomorphologic domains of Hellas that
436 emerges from this study suggests that the main period of deposition and reworking in the NW
437 interior of Hellas basin spanned the period between the Late Noachian- Early Hesperian and

Early Amazonian, consistent with previous studies (Tanaka and Leonard, 1995; Moore and Wilhelms, 2001 and 2007; Diot et al., 2014; Bernhardt et al., 2015). However, because the surface of our study area has experienced erosion over a large part (~4 Ga) of the Martian history, a precise dating of some of the domains is not possible. The surfaces of P1, P2, RT1 and RT2 display differences in the degree of erosion (Figs. 9 and 11). Indeed, P1 and P2 display smooth and knobby areas RT1 and RT2 present relatively rough-pitted ridges and smooth interiors. Due to this, the definition of a representative surficial texture for these domains is not possible. Concerning the RT2 domain, the narrow spatial extent consists of an additional issue for crater counting (e.g. Tanaka et al., 2014; Bernhardt et al., 2015). These points also result in atypical crater populations and non-representative age.

As such the correlation (Fig. 15) between the geomorphologic domains was essentially established based on the corresponding cross-cutting relationships described in section 4. Observations (e.g. Knob belts and pitted texture, buried craters) of areas of deep erosion (Fig. 8) presented in section 4.2 in combination with previous estimates of a Late Noachian-Early Hesperian age of emplacement for ACP (e.g. Tanaka and Leonard, 1995; Bernhardt et al., 2015) suggest that this domain is the oldest of Hellas. Likewise, cross-cutting relationships between the domains allow a refinement of the geomorphologic evolution of the NW Hellas. The major observations are (section 4): (i) P2 overlaps P1 (Fig. 9) ; (ii) P1 and necessary P2 cover some RT1 depressions (Figs. 10A1 and 10A2); (iii) P1 and necessary P2 are on the top of ACP in the eastern Hellas (Fig. S1 in supplementary material); (iv) P2 and RT2 ridges are deformed (twisted and curved) by the cells of the honeycomb terrain (Fig. 14). In addition, (v) spatial extension of RT2's ridges within P2 (Figs. 11B and 11C) and (vi) observations of boulders on the floor of RT2 as relic of P2 (Figs. 11A, 11B and 11C) suggest that RT2 formed through the erosion of P2. This is additionally supported by the concave shape and the multiple RT2 outcrops that are typical of an erosional landscape. Finally, (vii) the banded

material observed in some honeycomb cells (Fig. 7A1) may be remnants of a banded terrain infill. Consequently, the geomorphological history can be divided into three major episodes (Fig. 15): 1) emplacement of the ACP, 2) formation of RT1 followed by the plain deposits (P1 and P2) followed shortly by the formation of the RT2 and the honeycomb terrain domains, and 3) the formation of the banded terrain, structurally linked to the ACP. Thus the Amazonian-aged banded terrain (Diot et al., 2014) represents the last major depositional event in the NW interior of Hellas.

During the Amazonian, the geomorphic modifications have been mainly controlled by wind erosion, cryoturbation of the surface and remobilization of an ice-rich mantle deposit (Figs. 5 and 8B). We base this interpretation on the absence of any large domains post-dating or overlying the banded terrain. The observation of mega-ripples or small dunes with sharp crests in the inter-bands and triangular-shaped landforms on the top of the faults in the RT2 (Figs. 6A, 10B and 10C) is consistent with the occurrence of recent aeolian deposits and related erosional features. The tips of the triangular-shaped landforms, inferred to be caused by wind erosion, indicate a mostly SW-NE wind trend, which is consistent with wind-directions in NW Hellas as modeled by Howard et al. (2012). However, the lack of large dune fields and other major aeolian structures in this part of the basin suggests that wind erosion has been limited in extent (Howard et al., 2012). Likewise, the absence of aeolian features can also be due to the relative absence of readably mobilized sand sizes (very fine to fine sand). This latter interpretation may be supported by the thermal inertia values (300 – 450 tiu) obtained for the NW interior of Hellas, which are consistent with coarse grained sediment (very coarse sand to cobbles; Piqueux and Christensen, 2009). It should be noted that these particle sizes are larger than the ~ 1 μm-sized particle, which are the most-likely mobilized grains under present martian conditions (e.g. Read and Lewis, 2004).

The banded terrain is located in the latitudinal band (35°–55°) where Amazonian periglacial landforms have been extensively mapped on Mars (Squyres, 1979; Squyres and Carr, 1986; Head et al., 2005; Mangold, 2003; Milliken et al., 2003). Thus, the erosional features present on the surface of the bands including clusters of boulders, rockfalls, and periglacial features (Diot et al., 2014) suggest a combination of several periglacial erosional processes (Matsuoka, 1995; Head et al., 2011; Heldmann et al., 2013), cryoturbation and wind-induced abrasion, consistent with observations in terrestrial periglacial environments e.g., in the McMurdo Dry Valley, USA for example (Hall and Andre, 2001; Heldmann et al., 2013). For instance, the rockfalls and the clusters of boulders (Fig. 4) could have developed in response to mechanical weathering such as thermal cracking or sublimation processes. These features occur relatively often on the flanks of mountains on Earth (Giani, 1992; Valbuzzi et al., 2014). A possible initiation mechanism of these rockfalls is fracturing of rocks due to frost weathering and thermal contraction of the ground (Giani, 1992).

5.2. Possible origins of the domains

5.2.1. The plain deposits

Various hypotheses including volcanic and aqueous (e.g. Moore and Wilhelms, 2001; Bernhardt et al., 2015) origins for the widespread plain deposits (P1 and P2) have been previously proposed and are discussed in the following section. Table 2 summarizes the various origin hypotheses for each domain.

The smooth surfaces identified for the P1 and P2 domains could have originated through deposition of suspended material in a lake or may have been produced by the discharge of material from rivers, for instance through Dao or Harmakhis canyons (Moore and Wilhelms,

510 2001). We suggest this mainly because lacustrine deposits are mostly characterized by fine-
511 grained and stratified deposits. Likewise, aqueous environments on Earth, but also volcanic
512 settings are known to form analogous widespread relatively smooth surfaces. The relatively
513 low thermal inertia (200–300 tiu) acquired for P2 and P1 may favor this hypothesis, although
514 airfall dust may have affected these measurements. Recently, Bandfield et al., (2008 and
515 2013a) have detected amorphous hydrated silica in the western interior of Hellas close to P2
516 and P1. The formation of these minerals requires a relatively large amount of water
517 (Bandfield et al., 2013a). Due to the lack of other aqueous quartz, the amorphous form of the
518 hydrated silica and the sporadic spatial extent, Bandfield et al., (2013a) proposed a local
519 source of water confined to the west of Hellas to form these minerals. It is unlikely that the
520 P1 and P2 domains, considering their large spatial coverage (~142,000 km^2), would have
521 been deposited by an ephemeral and spatially localized water body. Moreover, we do not
522 observe light-toned layering or a stratified pattern within the P2 and P1 domains as observed
523 by Ansan et al., (2011) for the lacustrine deposits in the Terby crater. Finally, Crown et al.
524 (2005) noted a lack of fluvial landforms, which is inconsistent with the interpretation of
525 large-scale catastrophic flooding as formation mechanism for the plain deposits (at least P2)
526 in the eastern part of Hellas. Therefore, further investigations and additional HiRISE
527 coverage are necessary to validate or reject the hypothesis of a formation via suspension in a
528 lake.

529 Alternatively, effusive low viscosity lava flows such as the ones of the Etna or the Hawaiian
530 volcanoes (Hon. et al, 1994; Moore and Wilhelms, 2001; Bernhardt et al., 2015) can form
531 large basaltic-lava sheets. However, the relatively low thermal inertia (200–300 tiu) obtained
532 for the P2 and P1 domains is inconsistent with basaltic lavas, which typically reach 1,200 tiu
533 (e.g. Fergason et al., 2006a; Putzig and Mellon, 2007). A possible explanation for this large
534 difference is a post-depositional fragmentation of the material through physical weathering,

535 where the resulting debris may have a thermal inertia of <600 tiu (Bandfield et al., 2013b).
536 We note that such an origin for P1 and P2 would have further implications for interpreting
537 their structural and cross-cutting relationships with the neighboring honeycomb and the RT2
538 domains presented in section 4.3 and 4.4. In fact, despite their larger size (two to four orders
539 of magnitude), the surface texture of the honeycomb and RT2 domains are visually similar to
540 the surface in the northern Byers Peninsula in Antarctica (Moura et al., 2012), where multiple
541 freeze-thaw cycles have resulted in the formation of a patterned surface texture of volcanic
542 tuffs. However, the large distances to the closest observable volcanic source regions,
543 Amphitrites and Peneus Paterae (~1,400 km to the South) and Hadriacus Mons (~2,000 km to
544 the East) challenges the volcanic origin for the plain deposits.

545 Finally, formation of P1 and P2 through a combination of deposition, erosion and
546 remobilization (periglacial processes, wind abrasion for example) of a relatively young ice-
547 rich mantle deposit should be considered (e.g. Crown et al., 2005). Indeed, climatic models at
548 the planetary scale (e.g. Haberle et al., 2003; Forget et al., 2006; Madeleine et al., 2014)
549 showed that ice would accumulate in the region of Hellas during periods of high-obliquity.
550 Consequently, ice mixed with dust might form a thick ice-rich mantle layer in the mid-
551 latitudes as in the case of Malea Planum close to Hellas basin (e.g. Willmes et al., 2012;
552 Conway and Balme, 2014). Thermal inertia values of 200 tiu to 300 tiu, which are indicative
553 of fine-grained materials on the P1 and P2 surfaces, are consistent with this interpretation.

554

555 *5.2.2. The Honeycomb terrain*

556 In the case of the honeycomb terrain, Moore and Wilhelms (2001) proposed a formation by
557 soft-sediment deformation of waterlogged bottom sediment caused by the pressing of ice
558 within an ice-covered lake (Lowe, 1975; Allen, 1982). The low thermal inertia values (~400

559 tiu) for this domain indicate the presence of a fine to coarse-grained partially consolidated
560 material, which could have experienced soft-deformation. In addition, the lack of evidence
561 for brittle deformation (fractures, faults, etc.) combined with observations of local intensive
562 folding support the occurrence of soft or ductile deformation.

563 Based solely on the morphology of the honeycomb and RT2, a formation in response to the
564 rise of diapirs driven by buoyancy effects of salt (Fig. 16A) or plutons could provide
565 interesting viable alternatives (Mangold and Allemand, 2003; Leppänen et al., 2012;
566 Bernhardt et al., 2015). In the case of the hypothesis of the magmatic diapirs (Mangold and
567 Allemand, 2003; Lin, 2005), the general morphology of the honeycomb terrain (Fig. 7)
568 displaying ridges (relative highs) and oval depressions (relative lows) resembling the
569 Archean dome-and-basin structures (e.g. Bouhallier et al., 1995; Bloem et al., 1997; Chardon
570 et al., 1998; Mangold and Allemand, 2003; Lin, 2005). Triangles of intensive folding
571 between the oval shaped-plutons are observable in terrestrial Archean (~4 Ga) diapirs. The
572 formation of these folds is related to the anatexis upon magma emplacement, where the heat
573 of the rising magma results in the partial melting of the surrounding rocks. Such a mechanism
574 could explain the observed inter-honeycomb's cells areas of ductile deformation. However,
575 magmatic diapirism is commonly associated with large heat flows and intense deformation
576 over broader scales of several kilometers (e.g. Choukroune et al., 1995; Nadin et al., 1995;
577 Choukroune et al., 1997; Mège and Ernst, 2001). There is no evidence for tectonic
578 deformation at that scale in the Hellas basin. Unfortunately, we do not have quantitative data
579 about crustal heat flux or mineralogical assemblages indicative of high temperature
580 conditions to properly address this hypothesis. Nevertheless, we consider that the lack of
581 evidence for large-scale deformation in Hellas and the implication of very high heat flow
582 challenge this magmatic diapirism hypothesis as mechanism for the formation of the
583 honeycomb terrain.

584 Another hypothesis to consider is the salt diapirism. The rise of salt diapirs on Earth requires
585 weakening (mostly fracturing and erosion) of the overburden surface (Turcotte and Schubert,
586 1982; Mangold and Allemand, 2003; Hudec and Jackson, 2007; Talbot et al., 2009), which is
587 mainly accomplished in areas of active regional deformation (Vendeville and Jackson, 1992).
588 However, in the honeycomb area, we observe that the material between the honeycomb cells
589 is mainly folded and only few fractures can be identified. In addition, markers of intense
590 regional deformation are lacking in Hellas basin. Salt diapirism is commonly associated with
591 complex tectonic processes that can be divided in three stages: (i) "reactive", (ii) "active" and
592 (iii) "passive" diapirism (e.g. Nelson et al., 1989; Vendeville and Jackson, 1992). The intense
593 fracturing of the overburden surface enunciated above occurs in the "reactive" and "active"
594 phases while no fractures and local subsidence are observed during the "passive" stage (e.g.
595 Nelson, 1989; Vendeville and Jackson, 1992). Thus, reworking and erosion of the surface
596 posterior to the rise of the salt via, for instance, periglacial processes or wind activity, could
597 have removed part of the brittle structures, at least in our case. Accordingly, the honeycomb
598 terrain could reflect the local subsidence of the "passive" stage only. Although we cannot
599 fully address this question with the available data, we note that if such diapirism occurred in
600 waterlogged bottom sediment within a lake, then it could explain the morphology and ductile
601 deformation of the honeycomb and also the lack of clear signs of tectonism.

602 Finally, the ice diapirism hypothesis, proposed by Schenk and Jackson (1993, 2007) to
603 explain the Cantaloupe terrain on Neptune's icy-moon Triton (Fig. 16B) could potentially
604 explain the shape and texture of the honeycomb terrain. Despite their larger size (~40–50
605 km), the cells of the Cantaloupe terrain reveal a rough to hummocky interior with a smooth
606 elevated outer annulus similar to the honeycomb cells. Likewise, the intercellular material of
607 the Cantaloupe terrain is arranged as sigmoids (e.g. Schenk and Jackson, 1993, 2007) and
608 folds analogous to the features in the honeycomb terrain. Finally, the cantaloupe cells display

609 a spacing that is similar to that of the honeycomb cells. Schenk and Jackson (1993, 2007)
610 suggested a formation through a vertical flow of an over-pressured ice buried below the
611 surface. However we note that the similarities between the Cantaloupe and honeycomb
612 terrains are probably only morphological since the chemical properties and rheology of the
613 ice on Triton is not known. First, the composition of the Triton's ice is not well constrained
614 and may be made up of water and nitrogen, which is probably the major component of
615 Triton's surface (Schenk and Jackson, 1993, 2007). Second, at the very low surface
616 temperature (30–40 K) (e.g. Tryka et al., 1993) of Triton, the rheology of water and nitrogen
617 ice is unknown. Moreover, water ice diapirism has been suggested to explain the circular to
618 elliptical morphology of some depressions at the surface of Jupiter's icy-moon Europa (e.g.
619 Pappalardo et al., 1998; Rathbun et al., 1998). These features are 7–15 km in diameter, which
620 is in the range of the honeycomb cells, and they are relatively regularly spaced. Pappalardo et
621 al. (1998) proposed that these features are the manifestation of the rise of relatively warm
622 water ice masses through the thick ice-rich surface of Europa. Although morphological
623 differences exist between the features on Europa and the honeycomb cells (e.g. the absence of
624 an outer elevated boundary for the depressions on Europa), the overall landscape of the
625 Europa's fields of depressions do resemble the shape of the honeycomb terrain. It should be
626 noted that the surface in the Hellas basin is not mainly composed of ice. Therefore, the
627 surface manifestation of such ice diapirs is likely to be different than on Europa.

628

629 *5.2.3. Spatial extent of the banded terrain*

630 An extensive discussion about the mechanisms leading to the shape and surface texture of the
631 banded terrain has already been presented by Diot et al., (2014). Here, we discuss the spatial

relationships of the banded terrain with the domains that we have discussed in the previous chapters.

The cross-cutting relationships suggest that the origin of the banded terrain is structurally linked to the ACP. Likewise, the gradual contact between the honeycomb terrain and the banded terrain seems to reflect a northward progressive transition. In fact, previously reported mapping (Diot et al., 2014) shows that the concentric bands are generally located close to the honeycomb cells and display a global E-W orientation analogous to the honeycomb cells. In addition, Diot et al. (2014) suggested that the surface texture of the banded terrain formed in response to a northward-directed surficial viscous flow starting from the NW edge of the ACP. In this context, the observed E-W banded material within the honeycomb cells could have resulted from a deviation in flow direction as the banded terrain material hit the edges of the honeycomb cells. Thus the concentric bands could mask the presence of honeycomb cells that are filled by the viscous material of the banded flows. Further to the north, the honeycomb cells were apparently not completely filled with banded material as the corresponding material is only visible within the cells but not their margins (Fig. 7A1). Accordingly, the northernmost (~40 km to 60 km far from the concentric bands) honeycomb cells displaying no banded material (Fig. 7B) represent the northern boundary of the banded terrain flow.

We conclude that the possible flow of the banded terrain could have covered the NW interior of Hellas to a large extent. Moreover, the ambiguous concentric bands may be the result of interactions between the flowing material and the buried topography of the honeycomb unit.

6. Summary

In this study we analyzed the geomorphological assemblage of several domains mapped in the NW interior of Hellas.

Seven domains have been identified within the basin: the banded terrain, the central plateau named Alpheus Colles, two plain deposits (P1 and P2 domains), the reticulate terrains (RT1 and RT2 domains), and the honeycomb terrain. The analysis of the geomorphology of these domains and their correlation combined with ages previously estimated by other studies reveals that the major period of deposition in the interior of Hellas basin spans the period between the Late Noachian and the Amazonian. The newly acquired CTX and HiRISE images enable us to subdivide the plain deposits and reticulate domains into two subdomains each: P1, P2 and RT1, RT2. Consequently, we propose the following sequence of formation (from the oldest to the youngest): Alpheus Colles plateau, RT1, P1 and P2, RT2, honeycomb terrain and banded terrain (Fig. 15). We note however that the possible gradual transition between the honeycomb and the banded terrain shows that the banded terrain flow may have covered a larger part of the NW interior of Hellas than observed today.

We do not observe significant surface alteration post-dating the formation of the banded terrain indicating a relatively low level of geologic activity during the Amazonian in the NW Hellas. The conspicuous erosional surface expressions in the form of clusters of boulders, rockfalls or periglacial structures at the bands' surface suggest the occurrence of erosive processes in cold desert environments modifying the landscape. We suggest that the history of the basin can be divided into three major episodes: 1) formation of the ACP, 2) formation of RT1 followed by the plain deposits (P1 and P2) followed shortly by the formation of the RT2 and the honeycomb terrain domains, and 3) the formation of the banded terrain, structurally linked to the ACP. This implies that whatever process formed the banded terrain is the most recent major depositional process that shaped the NW interior Hellas basin to a large extent.

The newly-acquired thermal inertia data combined with the cross-cutting relationships allow the formulation of distinct hypotheses about the origins of formation of some of the domains. We tentatively favor an ice-rich volcanic debris or ice-dust mantle deposition during high-obliquity phases for P1 and P2 and ice diapirism for the honeycomb domain. Thus, ice-related processes seem to have significantly shaped the interior of the basin during its past history. This study thus shows that the suite of erosional and depositional processes leads to a complex surface architecture that can only be deciphered if high-resolution images are available.

Acknowledgments

XD would like to thank the Center for Space and Habitability of the University of Bern for funding and supporting this study. MR EL-M, NT, and FS are supported by funds from the Swiss National Science Foundation (SNSF). The stereo DTM processing was carried out at the UK NASA RPIF at University College London. The authors would like to thank Luca Guallini for discussion and a review of the paper. The authors would like also to thank Daniel Mège and an anonymous reviewer for their constructive reviews, which improved the manuscript overall.

References

Ahnert F., 1984. Local relief and the height limit of mountain ranges. American Journal of Science 284, 1035–1055.

Albee, A., 2002. The Mars Global Surveyor mission: description, status, and significant result. Highlights of Astronomy 12, 631–635.

Allen John, R., 1982. Sedimentary structures, their character and physical basis. Vol. 1, Elsevier.

Ansan, V., Mangold, N., Masson, P., Gailhardis, E. and Neukum, G., 2008. Topography of valley networks on Mars from Mars Express High Resolution Stereo Camera digital elevation models. Journal of Geophysical Research (Planets) 113, 7006.

Ansan, V., Loizeau, D., Mangold, N., Mouélic, S. L., Carter, J., Poulet, F., Dromart, G., Lucas, A., Bibring, J.–P., Gendrin, A., Gondet, B., Langevin, Y., Masson, P., Murchie, S., Mustard, J. and Neukum, G., 2011. Stratigraphy, mineralogy, and origin of layered deposits inside Terby crater, Mars. Icarus 211 (1), 273–304.

Bandfield, J. L., 2008. High–silica deposits of an aqueous origin in western Hellas basin, Mars. Geophysical Research Letters 35 (12).

Bandfield, J. L., Amador, E. S. and Thomas, N. H, 2013a. Extensive hydrated silica materials in western Hellas basin, Mars. Icarus 226 (2), 1489–1498.

Bandfield, J. L., Edwards, C. S., Montgomery, D. R. and Brand, B. D., 2013b. The dual nature of the martian crust: young lavas and old clastic materials. Icarus 222 (1), 188–199.

Berman, D. C., Crown, D. A. and Bleamaster, III, L.F., 2009. Degradation of mid–latitude craters on Mars. Icarus 200 (1), 77–95.

Berman, D. C., Crown. D. A. and Emily C. S. Joseph, 2015. Formation and mantling ages of lobate debris aprons on Mars: Insights from categorized crater counts. Planetary and Space Science (111), 83–99.

Bernhardt, H., Hiesinger, H., Ivanov, M. A., Ruesch, O., Erkeling, G., and Reiss, D., 2015. Photogeologic mapping and the geologic history of the Hellas basin floor, Mars. Icarus, doi:10.1016/j.icarus.2015.09.031.

Bleamaster, L.F., and Crown, D.A., 2010. Geologic Map of MTM -40277, -45277, -40272, and -45272 Quadrangles, Eastern Hellas Planitia region of Mars. U.S. Geological Survey Scientific Investigations Series Map 3096, scale 1:1,004,000.

Bloem, E. J., Dalstra, H. J., Ridley, J. R. and Groves, D. I., 1997. Granitoid diapirism during protracted tectonism in an Archaean granitoid–greenstone belt, Yilgarn Block, Western Australia. Precambrian Research 85, 147–171.

Bouhallier, H., Chardon, D. and Choukroune, P., 1995. Strain patterns in Archean dome-and-basin structures: the Dharwar craton (Karnataka, South India). Earth and Planetary Science Letters 135, 57–75.

Cabrol, N. A. and Grin, E. A., 2001. Composition of the drainage network on early Mars. Geomorphology 37, 269 – 287.

Cabrol, N. A. and Grin, E. A., 2010. Searching for lakes on Mars: Four decades of exploration. Nathalie A. Cabrol and Edmond A. Grin. Lakes on Mars, Elsevier, Amsterdam, 1–29.

Carr, M, 1995. The martian drainage system and the origin of valley networks and fretted channels. Journal of Geophysical Research 100, 7479–7507.

Carr, M. and Chuang, F., 1997. Martian drainage densities. Journal of Geophysical Research 102, 9145-9152.

Carter, J., Poulet, F., Bibring, J.–P., Mangold, N. and Murchie, S., 2013. Hydrous minerals on Mars as seen by the CRISM and OMEGA imaging spectrometers: updated global view.

746 Journal of Geophysical Research: Planets 118 (4), 831–858.
747 Chardon, D., Choukroune, P. and Jayananda, M., 1998. Sinking of the Dharwar basin (South
748 India): implications for Archean tectonics. Precambrian Research 91, 15–39.
749 Christensen P. R., 1986. The spatial distribution of rocks on mars. Icarus **68**: 217–238. DOI:
750 10.1016/0019-1035(86)90020-5.
751 Christensen, P. R., Jakosky, B. M., Kieffer, H. H., Malin, M., McSween, Jr., H. Y., Nealson,
752 K., Mehall, G., Silverman, S. and Ferry, S., 1999. The Thermal Emission Imaging System,
753 (THEMIS) Instrument for the 2001 Orbiter. Lunar and Planetary Science Conference,
754 Abstract 1470.
755 Christensen, P. R., Bandfield, J. L., Bell III, J. F., Gorelick, N., Hamilton, V. E., Ivanov, A.,
756 Jakosky, B. M., Kieffer, H., Malin, M. and others, 2003. Morphology and composition of
757 the surface of Mars: Mars Odyssey THEMIS results. Science 300, 2056.
758 Christensen, P. R., Jakosky, B., Kieffer, H., Malin, M., McSween, H. Y., Nealson, K.,
759 Mehall, G., Silverman, S., Ferry, S., Caplinger, M. and Ravine, M., 2004. The Thermal
760 Emission Imaging System, (THEMIS) for the Mars 2001 Odyssey Mission. Space Science
761 Reviews 110 (1–2), 85–130.
762 Chojnacki, M., Burr, D.M. and Moersch, J.E., 2014. Valles Marineris dune fields as
763 compared with other martian populations: Diversity of dune compositions, morphologies,
764 and thermophysical properties. Icarus 230, 151–161.
765 Choukroune, P., Bouhallier, H. and Arndt, N. T., 1995. Soft lithosphere during periods or
766 Archean crustal growth or crustal reworking. Geological Society, London, Special
767 publications 95, 67–86.
768 Choukroune, P., Ludden, J. N., Chardon, D., Calvert, A. J. and Bouhallier, H., 1997. Archean
769 crustal growth and tectonic processes: a comparison of the superior province, Canada and
770 the Dharwar craton, India. Geological Society, London, Special publications 121, 63–98.
771 Chuang, F.C., Noe Dobrea E. Z., Mest S. C. and Crown D. A., 2015. Geomorphologic
772 mapping andmineralogy of pits in intercrater plains, northwest circum-Hellas region,
773 Mars. Lunar and Planetary Science Conference, Abstract 2542.
774 Conway, S. J. and Balme, M. R., 2014. Decameter thick remnant glacial ice deposits on
775 Mars. Geophysical Research Letters 41 (15), 5402–5409.
776 Crown, D.A., Bleamaster, L.F., and Mest, S.C., 2005. Styles and timing of volatile-driven
777 activity in the eastern Hellas region of Mars. Journal of Geophysical Research 110,
778 E12S22, doi:10.1029/2005JE002496.
779 Crown, D. A., Bleamaster, L. F., Mest, S. C., Mustard, J. F., and Vincendon, M., 2010.
780 Geologic mapping of the NW rim of Hellas basin, Mars: Evidence for an Ancient Buried
781 Landscape. Lunar and Planetary Science Conference, 1888.
782 De Blasio, F., 2014. Investigating the hydrology of the alleged Hellas Planitia lake in
783 southern Mars. Lunar and Planetary Science Conference, Abstract 1511.
784 De Hon, R. A., 1992. Martian lake basins and lacustrine plains. Earth Moon and Planets 56,
785 95–122.
786 Diot, X., El–Maarry, M., Schlunegger, F., Norton, K., Thomas, N. and Grindrod, P., 2014.
787 The geomorphology and morphometry of the banded terrain in Hellas basin, Mars.
788 Planetary and Space Science 101 (0), 118–134.
789 Edwards, C. S., Nowicki, K. J., Christensen, P. R., Hill, J., Gorelick, N. and Murray, K.,
790 2011. Mosaicking of global planetary image datasets: 1. Techniques and data processing
791 for Thermal Emission Imaging System, (THEMIS) multi–spectral data. Journal of
792 Geophysical Research: Planets 116 (E10).
793 Ehlmann, B. L., Mustard, J. F., Murchie, S. L., Bibring, J.–P., Meunier, A., Fraeman, A. A.
794 and Langevin, Y., 2011. Subsurface water and clay mineral formation during the early
795 history of Mars. Nature 479, 53–60.

796 Ehlmann, B. L. and Edwards, C. S., 2014. Mineralogy of the martian surface. Annual Review
797 of Earth and Planetary Sciences 42 (1), 291–315.
798 El-Maarry M.R., W. Watters, N. McKeown, J. Carter, E. Noe Dobrea, J. Bishop, A.
799 Pommerol, N. Thomas, 2014. Putative Desiccation Cracks on Mars: A Synthesis from
800 Modeling, Analogue-Field Studies, and Global Observations, Icarus 241, 248–268.
801 Encrenaz, T., Fouchet, T., Melchiorri, R., Drossart, P., Gondet, B., Langevin, Y., Bibring, J.–
802 P., Forget, F. and Bézard, B., 2006. Seasonal variations of the martian CO over Hellas as
803 observed by OMEGA/Mars Express. Astronomy and Astrophysis 459, 265–270.
804 Fassett, C. I. and Head, III, J.W., 2008. The timing of martian valley network activity:
805 constraints from buffered crater counting. Icarus 195 (1), 61–89.
806 Fergason, R. L., Christensen, P. R., Bell, J. F., Golombek, M. P., Herkenhoff, K. E. and
807 Kieffer, H. H., 2006a. Physical properties of the Mars Exploration Rover landing sites as
808 inferred from Mini–TES "derived thermal inertia". Journal of Geophysical Research:
809 Planets 111 (E2).
810 Fergason, RL., Christensen, PR. and Kieffer, HH., 2006b. High-resolution thermal inertia
811 derived from the Thermal Emission Imaging System (THEMIS): thermal model and
812 applications. Journal of Geophysical Research **111** DOI: 10.1029/2006JE002735.
813 Forget, F., Haberle, R., Montmessin, F., Levrard, B. and Head, J., 2006. Formation of
814 glaciers on Mars by atmospheric precipitation at high obliquity. Science 311, 368-371.
815 Forsythe, R. and Blackwelder, C., 1998. Closed drainage crater basins of the Martian
816 highlands: constraints on the early martian hydrologic cycle, Journal of Geophysical
817 Research 103, 31421-31432.
818 Fortezzo, C. M. and Skinner, J. A., 2013. Geologic history of Runanga–Jorn basin, northeast
819 Hellas, Mars: based on modeled crater ages. Lunar and Planetary Science Conference,
820 Abstract 2104.
821 Giani, G. P., 1992. Rock slope stability analysis. CRC Press.
822 Gorelick, N. S., Weiss–Malik, M., Steinberg, B. and Anwar, S., 2003. JMARS: A
823 Multimission Data Fusion Application. S. Mackwell and E. Stansbery. Lunar and
824 Planetary Science Conference, Abstract 2057.
825 Graf, J. E., Zurek, R. W., Eisen, H. J., Jai, B., Johnston, M. and DePaula, R., 2005. The Mars
826 Reconnaissance Orbiter Mission. Acta Astronautica **57**, 566–578.
827 Grassi, D., Formisano, V., Forget, F., Fiorenza, C., Ignatiev, N., Maturilli, A. and Zasova, L.,
828 2007. The martian atmosphere in the region of Hellas basin as observed by the planetary
829 Fourier spectrometer, (PFS–MEX). Planetary and Space Science 55 (10), 1346–1357.
830 Grohmann C. H. and Riccomini C., 2009. Comparison of roving–window and search–
831 window techniques for characterizing landscape morphometry. Computers and
832 Geosciences 35, 2164–2169.
833 Haberle, R. M., McKay, C. P., Schaeffer, J., Cabrol, N. A., Grin, E. A., Zent, A. P. and
834 Quinn, R., 2001. On the possibility of liquid water on present–day Mars. Journal of
835 Geophysical Research: Planets 106 (E10), 23317–23326.
836 Haberle, R. M., Murphy, J. R. and Schaeffer, J., 2003. Orbital change experiments with a
837 Mars general circulation model. Icarus 161 (1), 66 – 89.
838 Hall, K. and André, M.–F., 2001. New insights into rock weathering from high–frequency
839 rock temperature data: an Antarctic study of weathering by thermal stress.
840 Geomorphology 41 (1), 23–35.
841 Head, J., Neukum, G., Jaumann, R., Hiesinger, H., Hauber, E., Carr, M., Masson, P., Foing,
842 B., Hoffmann, H., Kreslavsky, M., Werner, S., Milkovich, S., van Gasselt, S. and Team
843 HRSC, 2005. Tropical to mid-latitude snow and ice accumulation, flow and glaciation on
844 Mars. Nature 434, 346-351.
845 Head, J. W., Kreslavsky, M. A. and Marchant, D. R., 2011. Pitted rock surfaces on Mars: A

mechanism of formation by transient melting of snow and ice. Journal of Geophysical Research: Planets 116 (E9).
Heldmann, J., Pollard, W., McKay, C., Marinova, M., Davila, A., Williams, K., Lacelle, D. and Andersen, D., 2013. The high elevation Dry Valleys in Antarctica as analog sites for subsurface ice on Mars. Planetary and Space Science 85 (0), 53–58.
Hon, K., Kauahikaua, J., Denlinger, R. and Mackay, K., 1994. Emplacement and inflation of pahoehoe sheet flows: observations and measurements of active lava flows on Kilauea Volcano, Hawaii. Geological Society of America Bulletin 106 (3), 351–370.
Howard, A.; Moore, J. and Irwin, R., 2005. An intense terminal epoch of widespread fluvial activity on early Mars: 1. Valley network incision and associated deposits. Journal of Geophysical Research (Planets) 110 (E9), 12.
Howard, A. D., Spiga, A. and Moore, J. M., 2012. The deepest basin on Mars is formed by an aeolian erosion. Lunar and Planetary Science Conference, Abstract 1105.
Hubbard, B., Milliken, R. E., Kargel, J. S., Limaye, A. and Souness, C., 2011. Geomorphological characterisation and interpretation of a mid–latitude glacier–like form: Hellas Planitia, Mars. Icarus 211 (1), 330–346.
Hubbard, B., Souness, C. and Brough, S., 2014. Glacier-like forms on Mars. The Cryosphere, 8, 2047–2061, doi:10.5194/tc-8-2047-2014.
Hudec, M. R. and Jackson M. P. A., 2007. Terra infirma: understanding salt tectonics. Earth-Science Reviews 82, 1–28.
Kargel, J. S., Strom, R. G. and Johnson, N., 1991. Glacial geology of the Hellas Region on Mars. Lunar and Planetary Science Conference, Abstract 687.
Kirk, R. L., Howington-Kraus E., Redding B., Galuszka D., Hare T. M., Archinal B. A., Soderblom L. A. and Barrett J. M., 2003. High-resolution topomapping of candidate MER landing sites with Mars Orbiter Camera narrow-angle images. Journal of Geophysical Research, 108.
Kirk, R.L., Howington-Kraus, E., Rosiek, M.R., Anderson, J.A., Archinal, B.A., Becker, K. J., Cook, D.A., Galuszka, D.M., Geissler, P.E., Hare, T.M., Holmberg, I.M., Keszthe- lyi, L.P., Redding, B.L., Delamere, W.A., Gallagher, D., Chapel, J.D., Eliason, E.M., King, R., McEwen, A.S., 2008. Ultrahigh resolution topographic mapping of Mars with MRO HiRISE stereo images: meter-scale slopes of candidate Phoenix landing sites. Journal of Geophysical Research 113 (E3).
Kostama, V.P., Aittola, M., Raitala, J. and Цhman, T., 2001. The geology of the Hellas basin region: possible Mars Express HRSC target sites. AAS/Division for Planetary Sciences meeting, Abstracts 33.
Krause, M. O. and Grosfils, E. B., 2001. Analysis of Hellas rim geologic units using Mars Orbiter Laser Altimeter, (MOLA) Data. Lunar and Planetary Science Conference, Abstract 1108.
Leonard, G. J. and Tanaka, K. L., 1993. Hellas basin, Mars: formation by oblique impact. Lunar and Planetary Science Conference, pp. 867–868.
Leonard, G. J. and Tanaka, K. L., 2001. Geologic map of the Hellas region of Mars. U.S. Geological Survey Scientific Investigations Series Map I–2694, scale 1:5,000,000.
Leppänen, L. I., Kostama, V.–P. and Raitala, J., 2012. Oval structures on the floor of Hellas basin, Mars. Lunar and Planetary Science Conference, pp. 1784.
Lin, S., 2005. Synchronous vertical and horizontal tectonism in the Neoarchean: kinematic evidence from a synclinal keel in the northwestern Superior craton, Canada. Precambrian Research 139, 181–194.
Lowe, D., 1975. Water escape structures in coarse–grained sediments. Sedimentology 22, 157–204.
Madeleine, J.-B., J. W. Head, F. Forget, T. Navarro, E. Millour, A. Spiga, A. Colaïtis, A.

Määttänen, F. Montmessin, and J. L. Dickson, 2014. Recent ice ages on Mars: The role of radiatively active clouds and cloud microphysics. Geophysical Research Letter, 41, 4873–4879, doi:10.1002/2014GL059861.

Malin, M. C. and Edgett, K. S., 2000. Sedimentary rocks of early Mars. Science 290 (5498), 1927–1937.

Malin, M.C., Bell, J.F., Cantor, B.A., Caplinger, M.A., Calvin, W.M., Clancy, R.T., Edgett, K.S., Edwards, L., Haberle, R.M., James, P.B., Lee, S.W., Ravine, M.A., Thomas, P.C., Wolff, M.J., 2007. Context Camera Investigation on board the Mars reconnaissance orbiter. Journal of Geophysical Research 112 (E5).

Mangold, N., 2003. Geomorphic analysis of lobate debris aprons on Mars at Mars Orbiter Camera scale: evidence for ice sublimation initiated by fractures. Journal of Geophysical Research: Planets 108**,** (E4).

Mangold, N. and Allemand, P., 2001. Topographic analysis of features related to ice on Mars, Geophysical Research Letters 28 (3), 407–410.

Mangold, N. and Allemand, P., 2003. Ductile deformation in Hellas floor: salt diapirs or crustal domes? Sixth International Conference on Mars, pp. 3047.

Martin, T. Z. and Richardson, M. I., 1993. New dust opacity mapping from Viking infrared thermal mapper data. Journal of Geophysical Research: Planets 98 (E6), 10941–10949.

Matsubara, Y., Howard, A. D. and Gochenour, J. P., 2013. Hydrology of early Mars: valley network incision. Journal of Geophysical Research: Planets 118 (6), 1365–1387.

Matsuoka, N., 1995. Rock weathering processes and landform development in the Sor Rondane mountains, Antarctica. Geomorphology 12 (4), 323–339.

Maxwell, T. A. and Craddock, R. A., 1995. Age relations of martian highland drainage basins. Journal of Geophysical Research: Planets 100 (E6), 11765–11780.

McEwen, A. S., Delamere, W. A., Eliason, E. M., Grant, J. A., Gulick, V. C., Hansen, C. J., Herkenhoff, K. E., Keszthelyi, L., Kirk, R. L., Mellon, M. T., Squyres, S. W., Thomas, N. and Weitz, C., 2002. HiRISE: The High Resolution Imaging Science Experiment for Mars Reconnaissance Orbiter. Lunar and Planetary Science Conference, pp. 1163.

McEwen, A. S., Eliason, E. M., Bergstrom, J. W., Bridges, N. T., Hansen, C. J., Delamere, W. A., Grant, J. A., Gulick, V. C., Herkenhoff, K. E., Keszthelyi, L., Kirk, R. L., Mellon, M. T., Squyres, S. W., Thomas, N. and Weitz, C. M., 2007. Mars Reconnaissance Orbiters High Resolution Imaging Science Experiment, HiRISE. Journal of Geophysical Research: Planets 112 (E5).

McEwen, A. S., Banks, M. E., Baugh, N., Becker, K., Boyd, A., Bergstrom, J. W., Beyer, R. A., Bortolini, E., Bridges, N. T., Byrne, S., Castalia, B., Chuang, F. C., Crumpler, L. S., Daubar, I., Davatzes, A. K., Deardorff, D. G., DeJong, A., Delamere, W. A., Dobrea, E. N., Dundas, C. M., Eliason, E. M., Espinoza, Y., Fennema, A., Fishbaugh, K. E., Forrester, T., Geissler, P. E., Grant, J. A., Griffes, J. L., Grotzinger, J. P., Gulick, V. C., Hansen, C. J., Herkenhoff, K. E., Heyd, R., Jaeger, W. L., Jones, D., Kanefsky, B., Keszthelyi, L., King, R., Kirk, R. L., Kolb, K. J., Lasco, J., Lefort, A., Leis, R., Lewis, K. W., Martinez–Alonso, S., Mattson, S., McArthur, G., Mellon, M. T., Metz, J. M., Milazzo, M. P., Milliken, R. E., Motazedian, T., Okubo, C. H., Ortiz, A., Philippoff, A. J., Plassmann, J., Polit, A., Russell, P. S., Schaller, C., Searls, M. L., Spriggs, T., Squyres, S. W., Tarr, S., Thomas, N., Thomson, B. J., Tornabene, L. L., Houten, C. V., Verba, C., Weitz, C. M. and Wray, J. J., 2010. The High Resolution Imaging Science Experiment, (HiRISE) during MRO Primary Science Phase, (PSP). Icarus 205 (1), 2–37.

Mellon, M. T., Jakosky, B. M., Kieffer, H. H. and Christensen, P. R., 2000. High-resolution thermal inertia mapping from the Mars Global Surveyor Thermal Emission Spectrometer. Icarus 148, 437–455.

Mège, D. and Ernst, R. E., 2001. Contractional effects of mantle plumes on Earth, Mars, and

946 Venus. Geological Society of America Special paper 352, 103–140.
947 Mest, S. C., Crown, D.A. and Harbert, W., 2001. Highland drainage basins and valley
948 networks in the eastern Hellas region of Mars. 32nd Lunar and Planetary Science, abstract
949 #1457.
950 Mest, S. C. and Crown, D. A., 2005. Millochau crater, Mars: infilling and erosion of an
951 ancient highland impact crater. Icarus 175 (2), 335 – 359.
952 Mest, S.C., and Crown, D.A., 2006. Geologic Map of MTM -20272 and -25272 Quadrangles,
953 Tyrrhena Terra region of Mars. U.S. Geological Survey Scientific Investigations Series
954 Map 2934, scale 1:1,004,000.
955 Mest, S.C., Crown, D.A., and Harbert, W., 2010. Watershed modeling in the Tyrrhena Terra
956 region of Mars. Journal of Geophysical Research 115, E09001,
957 doi:10.1029/2009JE003429.
958 Milliken, R. E., Mustard, J. F. and Goldsby, D. L., 2003. Viscous flow features on the surface
959 of Mars: observations from high–resolution Mars Orbiter Camera, (MOC) images. Journal
960 of Geophysical Research: Planets 108 (E6).
961 Moore, J. M. and Edgett, K. S., 1993. Hellas Planitia, Mars: Site of net dust erosion and
962 implications for the nature of basin floor deposits. Geophysical Research Letters 20 (15),
963 1599–1602.
964 Moore, J. M. and Wilhelms, D. E., 2001. Hellas as a possible site of ancient ice–covered
965 lakes on Mars. Icarus 154 (2), 258–276.
966 Moore, J. M. and Howard, A. D., 2005. Layered deposits and pitted terrain in the Circum
967 Hellas region. 36th Annual Lunar and Planetary Science Conference, pp. 1512.
968 Moore, J. M. and Wilhelms, D. E., 2007. Geologic map of a part of western Hellas Planitia,
969 Mars, U.S. Geological Survey Scientific Investigations Map 2953, scale 1:1,004,000.
970 Moura, P. A., Francelino, M. R., Schaefer, C. E. G., Simas, F. N. and de Mendon, B. A.,
971 2012. Distribution and characterization of soils and landform relationships in Byers
972 Peninsula, Livingston Island, Maritime Antarctica. Geomorphology 156 (0), 45–54.
973 Murchie, S., Arvidson, R., Bedini, P., Beisser, K., Bibring, J.–P., Bishop, J., Boldt, J.,
974 Cavender, P., Choo, T., Clancy, R. T., Darlington, E. H., Des Marais, D., Espiritu, R.,
975 Fort, D., Green, R., Guinness, E., Hayes, J., Hash, C., Heffernan, K., Hemmler, J., Heyler,
976 G., Humm, D., Hutcheson, J., Izenberg, N., Lee, R., Lees, J., Lohr, D., Malaret, E., Martin,
977 T., McGovern, J. A., McGuire, P., Morris, R., Mustard, J., Pelkey, S., Rhodes, E.,
978 Robinson, M., Roush, T., Schaefer, E., Seagrave, G., Seelos, F., Silverglate, P., Slavney,
979 S., Smith, M., Shyong, W.–J., Strohbehn, K., Taylor, H., Thompson, P., Tossman, B.,
980 Wirzburger, M. and Wolff, M., 2007. Compact Reconnaissance Imaging Spectrometer for
981 Mars, (CRISM) on Mars Reconnaissance Orbiter, MRO. Journal of Geophysical Research:
982 Planets 112, E05S03, doi:10.1029/2006JE002682.
983 Nadin, P. A., Kusznir, N. J. And Toth, J., 1995. Transient regional uplift in the early Tertiary
984 of the northern Notrh Sea and the development of Iceland plume. Geological Society
985 Journal 152, 953–958.
986 Nelson, T. H., 1989. Style of salt diapirs as a function of the stage of evolution and the nature
987 of the encasing sediments. In Gulf of Mexico salt tectonics, associated processes and
988 exploration potential: Gulf Coast Section SEPM Foundation Tenth Annual Research
989 Conference, pp. 109–110.
990 Ormö, J. and Komatsu, G., 2003. Mars Orbiter Camera observation of linear and curvilinear
991 features in the Hellas basin: indications for multiple processes of formation. Journal of
992 Geophysical Research: Planets 108, 5059, doi:10.1029/2002JE001980 (E6).
993 Osterloo, M. M., Hamilton, V. E., Bandfield, J. L., Glotch, T. D., Baldridge, A. M.,
994 Christensen, P. R., Tornabene, L. L. and Anderson, F. S., 2008. Chloride–bearing
995 materials in the southern highlands of Mars. Science (319), 1651–1654.

Osterloo, M. M., Anderson, F. S., Hamilton, V. E. and Hynek, B. M., 2010. Geologic context of proposed chloride–bearing materials on Mars. Journal of Geophysical Research: Planets 115, E10012, doi:10.1029/2010JE003613.

Pappalardo, R., Head, J. W., Greeley, R., Sullivan, R. J., Pilcher, C., Schubert, G., Moore, W. B., Carr, M. H., Moore, J. M., Belton, M. J. S. and Goldsby, D. L., 1998. Geological evidence for solid-state convection in Europa's ice shell. Nature 391, p. 365.

Pierce, T. L. and Crown, D. A., 2003. Morphologic and topographic analyses of debris aprons in the eastern Hellas region, Mars. Icarus (163), 46–65.

Piqueux, S. and Christensen, PR., 2009. A model of thermal conductivity for planetary soils: 1. Theory for unconsolidated soils. Journal of Geophysical Research **114** DOI: 10.1029/2008JE003308

Plaut, J. J., 2003. The Mars Odyssey Science Mission. AGU, Abstracts A1.

Putzig, N. E. and Mellon, M. T., 2007. Apparent thermal inertia and the surface heterogeneity of Mars. Icarus 191 (1), 68–94.

Rathbun, J. A., Musser Jr., G. S. and Squyres, S. W., 1998. Ice diapirs on Europa: implications for liquid water. Geophysical Research Letters 25, 4157–4160.

Read, P.L. and Lewis, S. R., 2004. The martian climate revisited: atmosphere and environment of a desert planet. Springer Science & Business Media.

Ruff, SW., and Christensen P. R., 2002. Bright and dark regions on Mars: particle size and mineralogical characteristics based on Thermal Emission Spectrometer data. J. Geophys. Res. **107** DOI: 10.1029/2001JE001580.

Schenk, P. and Jackson, M. P. A., 1993. Diapirism on Triton,a record of crustal layering and instability. Geology 21, 299–302.

Schenk, P. M. and Zahnle, K., 2007. On the negligible surface age of Triton. Icarus 192 (1), 135–149.

Simpson, R. A., Tyler, G. L., Brenkle, J. P. and Sue, M., 1979. Viking bistatic radar observations of the Hellas basin on Mars–Preliminary results. Science (203), 45.

Smith, D. E., Zuber, M. T., Solomon, S. C., Phillips, R. J., Head, J. W., Garvin, J. B., Banerdt, W. B., Muhleman, D. O., Pettengill, G. H., Neumann, G. A., Lemoine, F. G., Abshire, J. B., Aharonson, O., David, C., Brown, Hauck, S. A., Ivanov, A. B., McGovern, P. J., Zwally, H. J. and Duxbury, T. C., 1999. The Global Topography of Mars and Implications for Surface Evolution. Science 284 (5419), 1495–1503.

Smith, D. E., Zuber, M. T., Frey, H. V., Garvin, J. B., Head, J. W., Muhleman, D. O., Pettengill, G. H., Phillips, R. J., Solomon, S. C., Zwally, H. J., Banerdt, W. B., Duxbury, T. C., Golombek, M. P., Lemoine, F. G., Neumann, G. A., Rowlands, D. D., Aharonson, O., Ford, P. G., Ivanov, A. B., Johnson, C. L., McGovern, P. J., Abshire, J. B., Afzal, R. S. and Sun, X., 2001. Mars Orbiter Laser Altimeter: Experiment summary after the first year of global mapping of Mars. Journal of Geophysical Research: Planets 106 (E10), 23689–23722.

Souness, C., Hubbard, B., Milliken, R. E. and Quincey, D., 2012. An inventory and population–scale analysis of martian glacier–like forms. Icarus 217 (1), 243–255.

Squyres, S. W., 1979. The distribution of lobate debris aprons and similar flows on Mars. Journal of Geophysical Research: Solid Earth 84 (B14), 8087–8096.

Squyres, S. W. and Carr, M. H., 1986. Geomorphic Evidence for the Distribution of Ground Ice on Mars. Science 231(4735), 249–252.

Talbot, C. J. and Pohjola, V., 2009. Subaerial salt extrusions in Iran as analogues of ice sheets, streams and glaciers. Earth–Science Reviews 97, 155–183.

Tanaka, K. L. and Leonard, G. J., 1995. Geology and landscape evolution of the Hellas region of Mars. Journal of Geophysical Research: Planets 100 (E3), 5407–5432.

Tanaka, K.L., Robbins, S.J., Fortezzo, C.M., Skinner Jr, J.A. and Hare, T.M., 2014. The

digital global geologic map of Mars: chronostratigraphic ages, topographic and crater morphologic characteristics, and updated resurfacing history. Planetary and Space Science 95, 11–24.
Tryka, K. A., Brown, R. H., Anicich, V. Cruikshank, D. P. and Owen, T. C., 1993. Spectroscopic determination of the phase composition and temperature of nitrogen ice on Triton. Science 261, 751–754.
Turcotte, D. L. and Schubert, G., 1982. Geodynamics: applications of continuum physics to geological problems, 450 pp.
Valbuzzi, E., Crosta, G.B. and De Blasio, F.V., 2014. Probable rock falls in the pits of Arsia Mons, Mars. Lunar and Planetary Science Conference, Abstract 2093.
Vendeville, B. Ci. And Jackson, P. A., 1992. The rise of diapirs during thin-skinned extension. Marine and Petroleum Geology 9, 331–354.
Werner, S., 2008. The early martian evolution: constraints from basin formation ages. Icarus 195 (1), 45–60.
Willmes, M., Reiss, D., Hiesinger, H. and Zanetti, M., 2012. Surface age of the ice-dust mantle deposit in Malea Planum, Mars, Planetary and Space Science 60 (1), 199 – 206.
Wilson, S.A., Howard, A.D., Moore, J.E., and Grant, J.A., 2007. Geomorphic and stratigraphic analysis of crater Terby and layered deposits north of Hellas basin, Mars. Journal of Geophysical Research 112, E08009.
Wilson, S. A., Moore, J. M., Howard, A. D. and Wilhelms, D. E.Cabrol, N. A. and Grin, E. A., 2010. Evidence for ancient lakes in the Hellas region. Lakes on Mars, Elsevier BV, 195–222.
Wilson, S. A., Grant, J. A. and Howard, A. D., 2012. Distribution of intracrater alluvial fans and deltaic deposits in the southern highlands of Mars. Lunar and Planetary Science Conference, Abstract 2462.

Tables and Figure captions

Table 1. *Table of the values of thermal inertia used in this study to determine the composition (grain-size) of the different domains (image IDs, location and range of values with the standard deviation).*

Table 2 (origin hypotheses). *Table summarizing the various hypotheses of formation for the different domains of the NW of Hellas. This table provides the general morphology of each domains, the cross-cutting relationships between the domains and the possible formations mechanisms of the domains. The favored mechanism of formation is highlighted in the row "formations mechanism(s)".*

Figure 1. *(A) THEMIS day IR with MOLA colors map of the NW Hellas basin, which is our study area. The color outlines represent the different units for clarity. Colored outlines are: the Alpheus Colles plateau (red), the banded terrain (blue), the Honeycomb terrain (green), the reticulate terrain 1 (yellow), the reticulate terrain 2 (orange), the plain deposit 1 (black with dashed lines), and the plain deposit 2 (pink). The white boxes indicate the location of the other figures of this paper. The inset (B) represents a general THEMIS day IR map overlaid with MOLA color elevation map of the Hellas basin. The white box on this inset indicates the location of the Fig. 1A. (C) MOLA shaded relief map of the NW of the Hellas basin with white boxes that indicate the location of the other figures of the paper (example: "8A" shows the position of the figure 8A of the paper).*

Figure 2. *CTX views of the different morphologies of banded terrain. (A) Linear bands (images IDs: P17_007768_1371, B18_16642_1371; image center: 42.6°S, 52.2°E); (B) Concentric bands (image IDs: P19_008559_1408, P17_007557_1386; image center: 39.4°S, 53.2°E); (C) Lobate bands, which are underlined by the white dashed lines (image ID: P17_007768_1371; image center: 41.4°S, 51.7°E).*

Figure 3. *Example of HiRISE images showing the texture of the surface of the bands. (A) HiRISE view (image ID: ESP_033560_1395; image center: 40.4°S, 51.8°E) showing numerous clusters of boulders on the surface of a band; (B) HiRISE view (image ID: PSP_010563_1410; image center: 38.8°S, 55.5°E) presenting an example of a halo of boulders around a fresh impact crater.*

Figure 4. *HiRISE view (image ID: PSP_006133_1410; image center: 38.7°S, 54.4°E) showing a typical rockfall, which starts from the boundary of a lobate band. The blocks near the band are larger than the one at the end of the slope. Thus, the size of the falling blocks decreases away of the band.*

Figure 5. *HiRISE image (image ID: PSP_007623_1385; image center: 41.2°S, 51.2°E) presenting the footprint of a viscous flow feature similar to the others observed on Mars as in the east of Hellas. (A) This HiRISE view presents the entire structure of the viscous flow. The nomenclature used is the one of Milliken et al. (2003): p.l for principal lobe, f.r: front ridges; (B) This HiRISE (same image) close up of the top of the structure reveals the presence of multiple boulders; (C) and (D) two HiRISE close-up of the termination of the viscous flow feature revealing the presence of the front ridges (fr) and terminal polygons respectively.*

Figure 6. *(A) HiRISE observation (image ID: PSP_006278_1410; image center: 38.8°S, 55.5°E) displaying possible dunes in the inter-bands; (B) HiRISE image (image ID: ESP_028589_1380; image center: 41.6°S, 51.8°E) showing an example of the detachment of the band from a high-standing terrain, in this case the high-standing terrain is a part of the NW margin of the Alpheus Colles plateau.*

Figure 7. *CTX views presenting some honeycomb cells close to the banded terrain (A1 and A2) and others farther to the north of the banded terrain (B). On (A1) the cells display a banded material analogous to the linear bands (image ID: P17_007781_1414 and P15_006779_1414, B21_017710_1425; image A center: 36.9°S, 55.6°E). The close-up 8A2)*

of the same CTX image shows the structures (pointed by white arrows) that can be interpreted as layers in the honeycomb cell; and on (B) the honeycomb cells display a smooth to hummocky surface (images IDs B: P17_007860_1462 and P19_008361_1443; image B center: 35.2°S, 58.6°E).

Figure 8. *(A) CTX view (image IDs: B19_017011_1358, P19_008506_1359; image center: 41.5°S, 59.5°E) of the layered knobs visible on the surface of the Alpheus Colles plateau. The layers are highlighted by white arrows. A sketch of the knobs indicated by the numbers 1, 2, 3 to illustrate the stack of layers is given on the right; (B) THEMIS daytime view of a lobate feature located on the top of the Alpheus Colles plateau (image center: 40.1°S, 68.3°E).*

Figure 9. *CTX views (A1, A2 and B1) and sketch (B2) showing the cross-cutting relationships between the plain deposit 1 (P1) and the plain deposit 2 (P2). (A1) CTX image (image ID: B19_016919_1421, B19_017130_1422; image center: 39.37°S, 51.6°E) that shows P2 overlapping P1, the white arrows indicate the contact P1-P2; (A2) CTX close-up (image ID: B19_016919_1421) of the contact P1-P2 indicated by a white box on the Fig. 9A1, the white arrows show the morphological transition where P2 overlies P1; (B1) CTX observation (image ID: P19_008269_1420, B19_016919_1421, B19_017130_1422; image center: 38.5°S, 51.5°E) that displays another example of the cross-cutting relationships between P1 and P2. On this image, the white arrows underline the contact P1-P2*

Figure 10. (A1) *CTX view (image ID: P17_007834_1426 and P19_008625_1425; image center: 37.5°S, 48.7°E) showing the contact between the RT1 and P1. In this figure, the P1 covers the RT1. The white box represent the location of the sketch (A2) located on the left of the CTX observation (A1). On (A2), the contact RT1-P1 is showed by the thicker white line. The white dashed lines on (A2) indicates the ridges of RT1 apparently covered by P1; (B) HiRISE view and a close-up (C) of the same image (image ID: PSP_008058_1415, image center: 38.1°S, 52.9°E) showing a possible fault network observed in RT2.*

Figure 11. *HiRISE views (image ID: PSP_008058_1415; image center: 38.1°S, 52.9°E) showing the contact between the RT2 and P2. (A) This HiRISE observation of the same image shows a degradation of P2 forming the RT2. The surface of RT2 displays boulders as relic of the texture of P2; (B) HiRISE view of the same image revealing the imbrication of the ridges of RT2 within the P2. We can observe that the ridges of RT2 propagate into the P2 and (C) close up showing the imbrication of RT2 ridges within the P2.*

Figure 12. *(A) HiRISE DTM's hillshade where the grayscale shows the illumination and (B) slope map of the same DTM where the red color indicates the higher slopes and the blue color shows gentler slope to flat terrains. The ridges and the floor of the depressions reveal a bluish color indicative of a flat surface, whereas near to the ridges the color is red indicative of high slopes. DTM built from the HiRISE image pair: ESP_024936_1435 and ESP_033494_1435.*

Figure 13. *Relief map on the left associated with profiles perpendicular to the ridges of RT2 on the right (A-A', B-B'). On these two profiles, we can note the relief of the depressions in the range 15–20 m. DTM built from the HiRISE image pair: ESP_024936_1435 and ESP_033494_1435.*

Figure 14. *CTX views showing the complex cross-cutting relationships between: the honeycomb terrain (noted HC), the plain deposit 2 (P2) and the reticulate terrain 2 (RT2). (A) On this CTX image (image ID: P14_006700_1386; image center: 38.8°S, 52.6°E) the bulging material that forms the ridges of the HC cells seems to be made up of P2 material indicative of a reworking, a modification of P2 by the formation of the honeycomb terrain. (B1) This CTX observation illustrates the deformation of the ridges of RT2 by the honeycomb cells (image ID: P18_008058_1438; image center: 38.3°S, 53.02°E). We can observe that some of the ridges of RT2 are twisted in contact with the honeycomb cells (HC). In addition some depressions of RT2 have a pinched-shape between two honeycomb cells as it is showed*

on the sketch B2. On the sketch B2 in the bottom right corner, the cells of the honeycomb are represented by the dashed areas and the ridges of RT2 by the white lines.

Figure 15. *Schema of the relative correlation of the different geomorphologic domains mapped and characterized in this study of the interior of the NW Hellas basin. This reconstruction is based on the cross-cutting relationships and geometric interactions between the different domains.*

Figure 16. (A) *Google Earth view showing an example of salt diapirs observable in Iran (Great Kavir salt diapirs); (B) Typical observation of the surface of the Neptune's moon Triton illustrating the Cantaloupe terrain (image credit: JPL/NASA/Voyager 2). These oval shapes have been interpreted has ice-diapirs formed due to the extrusion of an over-pressured ice below the surface.*

FIG1

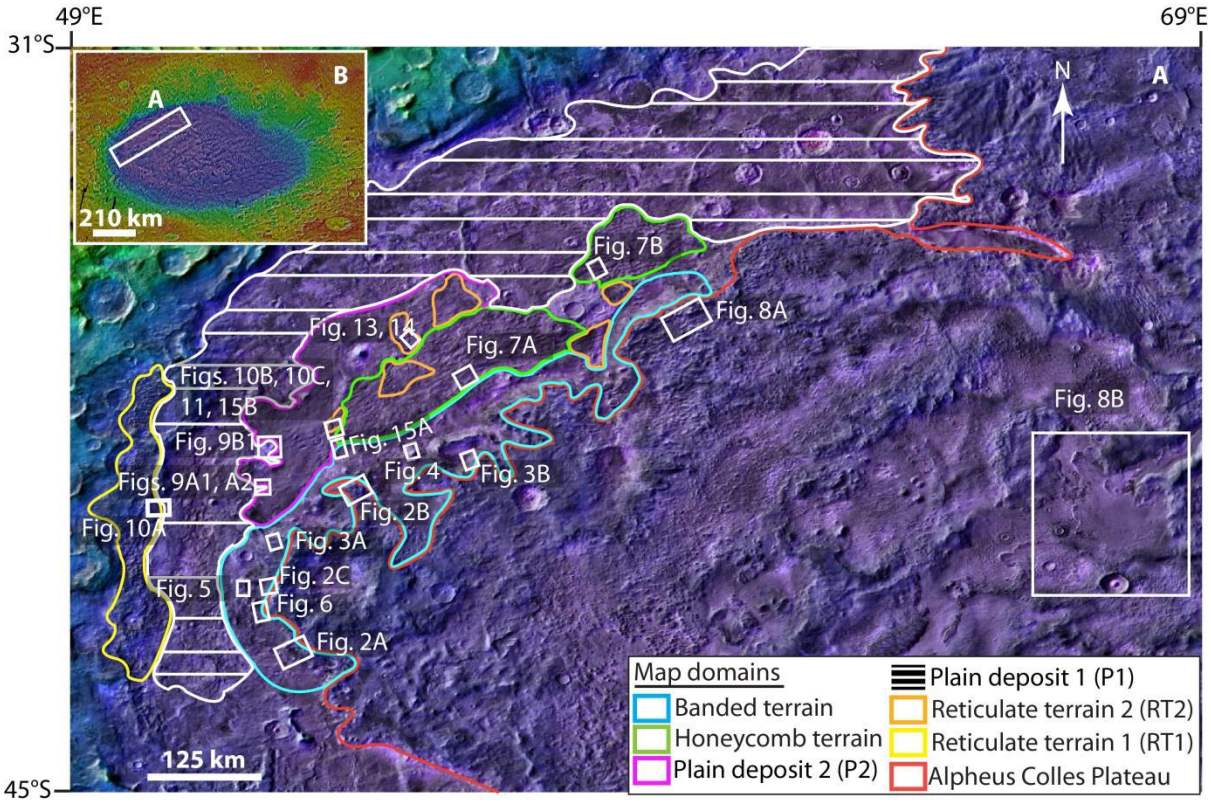
49°E
69°E
31°S
45°S
A
B
210 km
N
A
Fig. 7B
Fig. 8A
Fig. 13, 14
Fig. 7A
Figs. 10B, 10C, 11, 15B
Fig. 9B1
Fig. 15A
Figs. 9A1, A2
Fig. 4
Fig. 3B
Fig. 10A
Fig. 2B
Fig. 3A
Fig. 5
Fig. 2C
Fig. 6
Fig. 2A
Fig. 8B
125 km
Map domains
Banded terrain
Honeycomb terrain
Plain deposit 2 (P2)
Plain deposit 1 (P1)
Reticulate terrain 2 (RT2)
Reticulate terrain 1 (RT1)
Alpheus Colles Plateau

FIG2

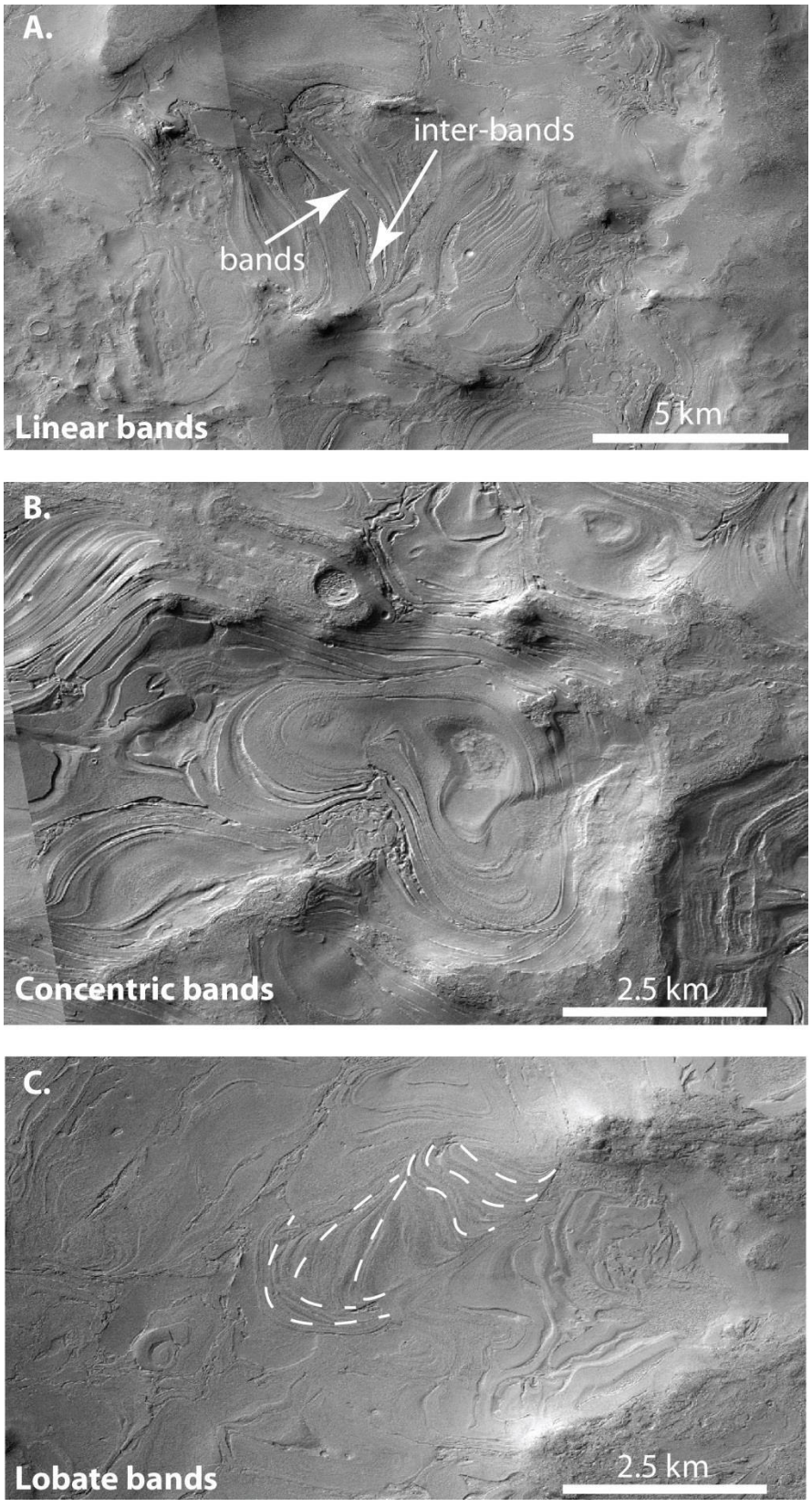
A.
inter-bands
bands
Linear bands
5 km
B.
Concentric bands
2.5 km
C.
Lobate bands
2.5 km

FIG3

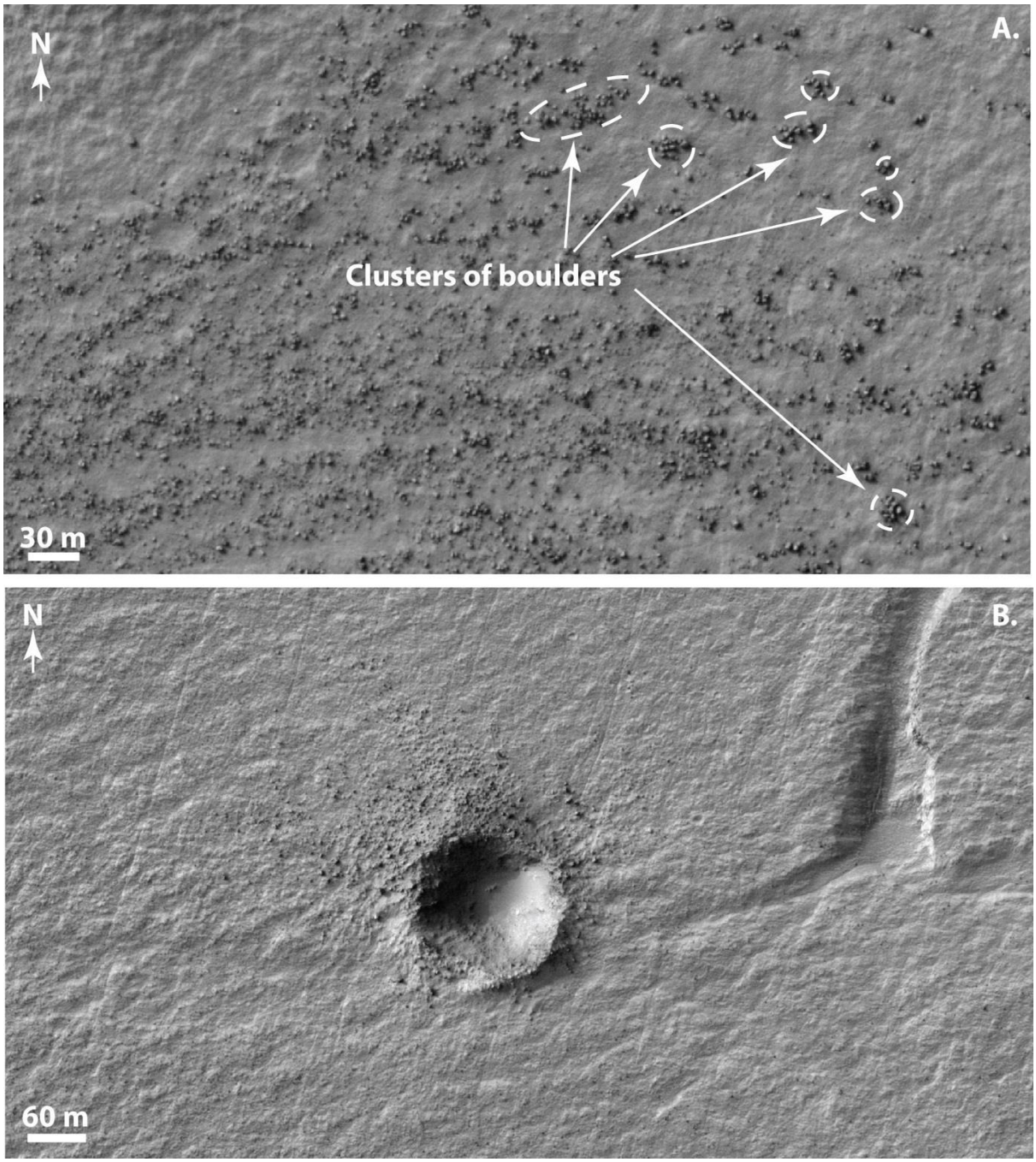

FIG4

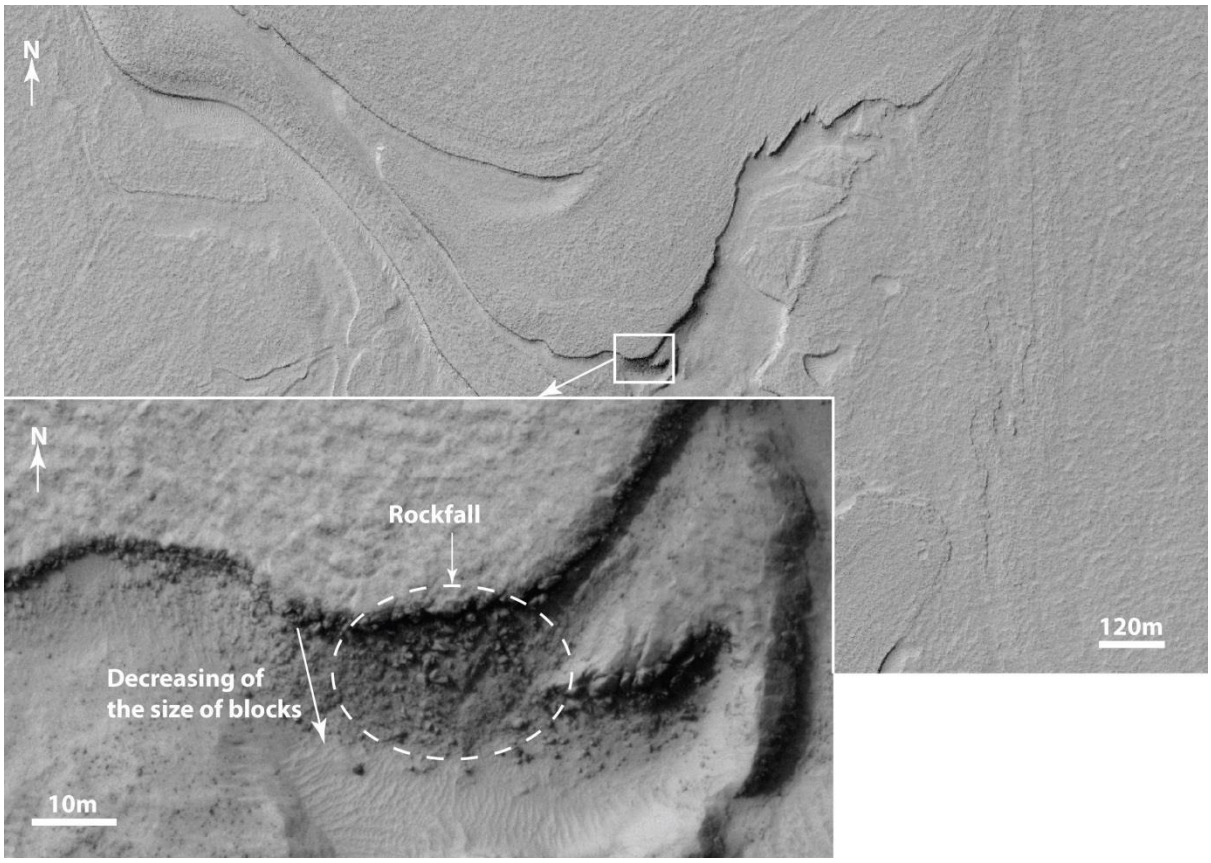
N
N
Rockfall
Decreasing of
the size of blocks
10m
120m

FIG5

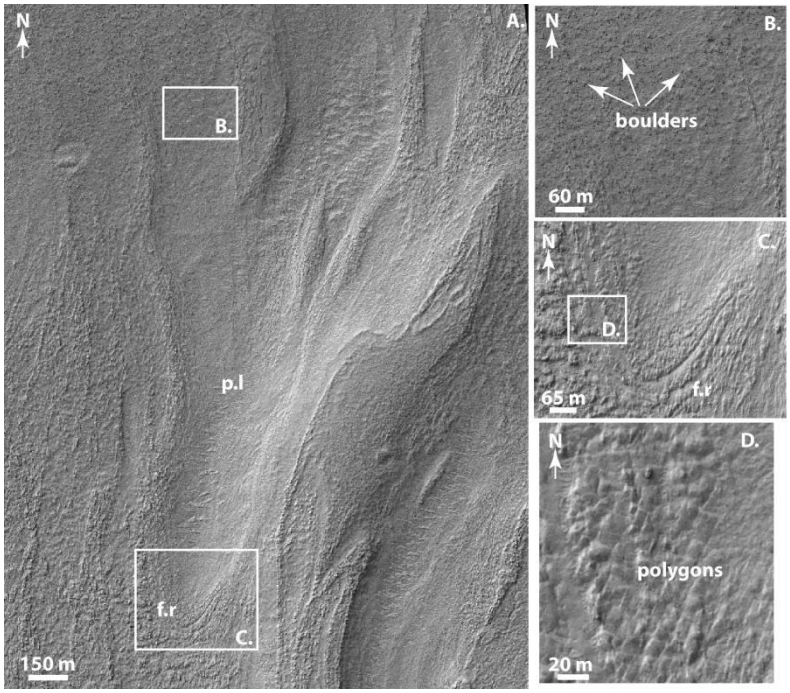
N
A.
B.
p.l
f.r
C.
150 m
N
B.
boulders
60 m
N
C.
D.
65 m
f.r
N
D.
polygons
20 m

FIG6

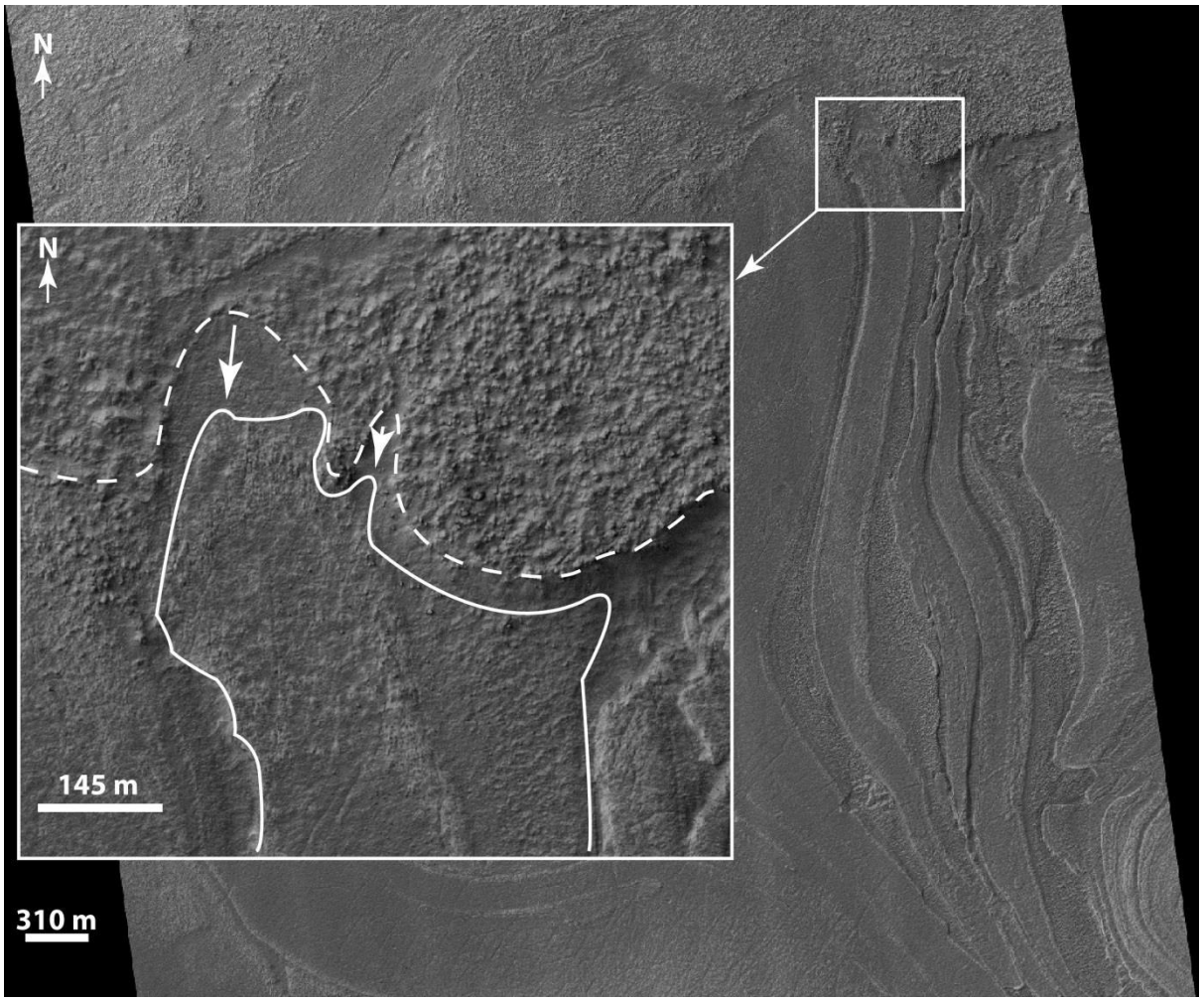

FIG7

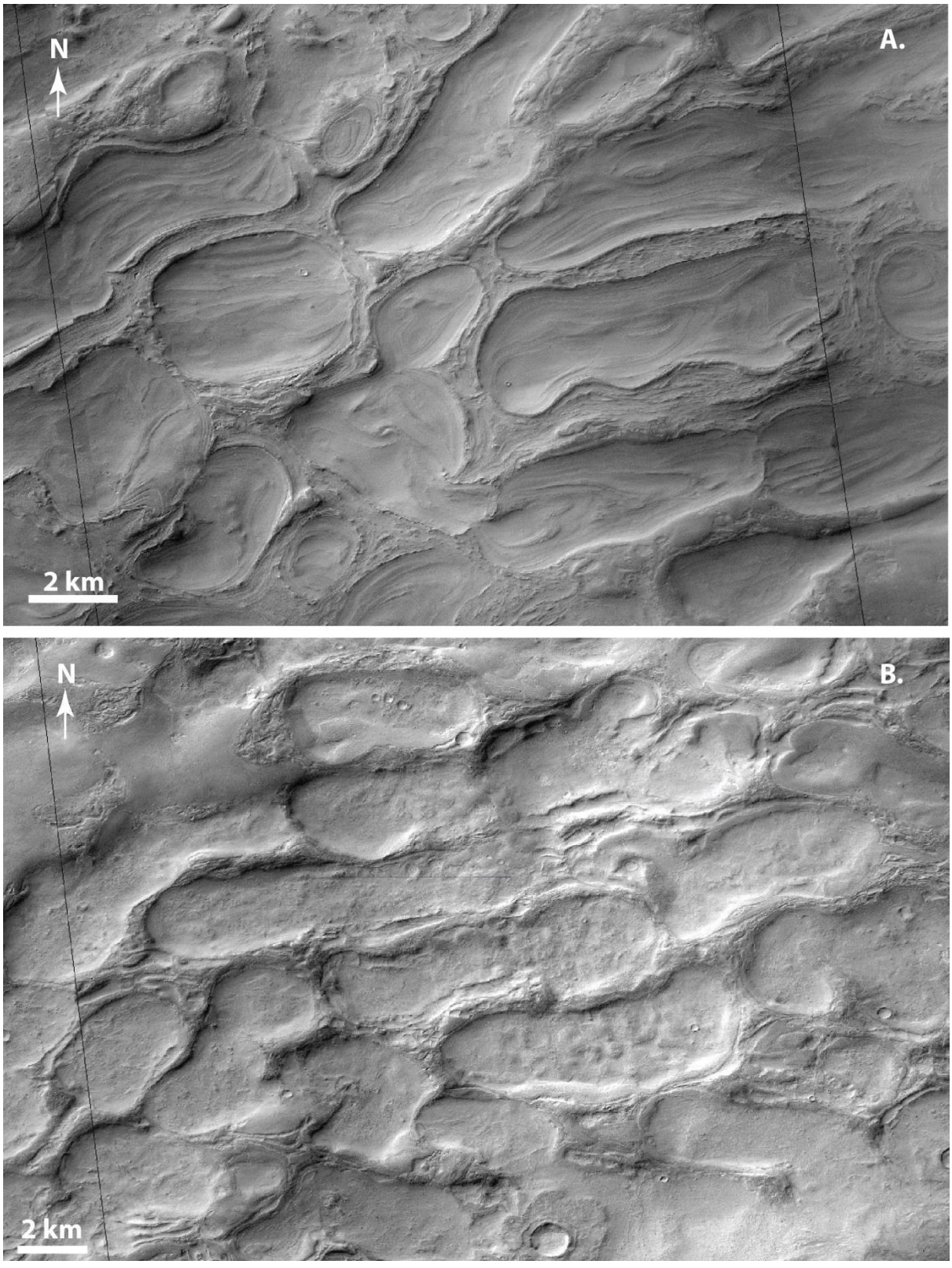

FIG8

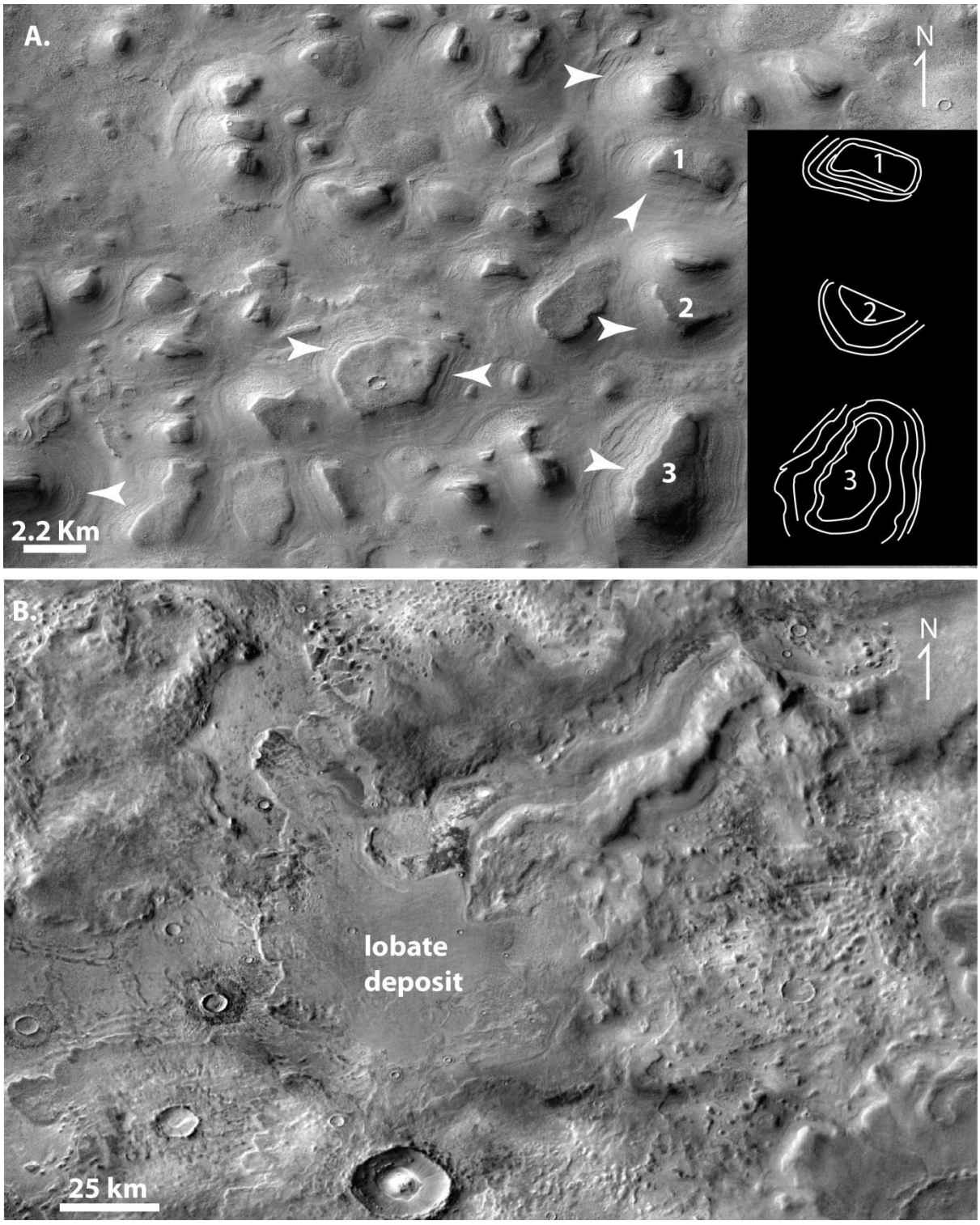

FIG9

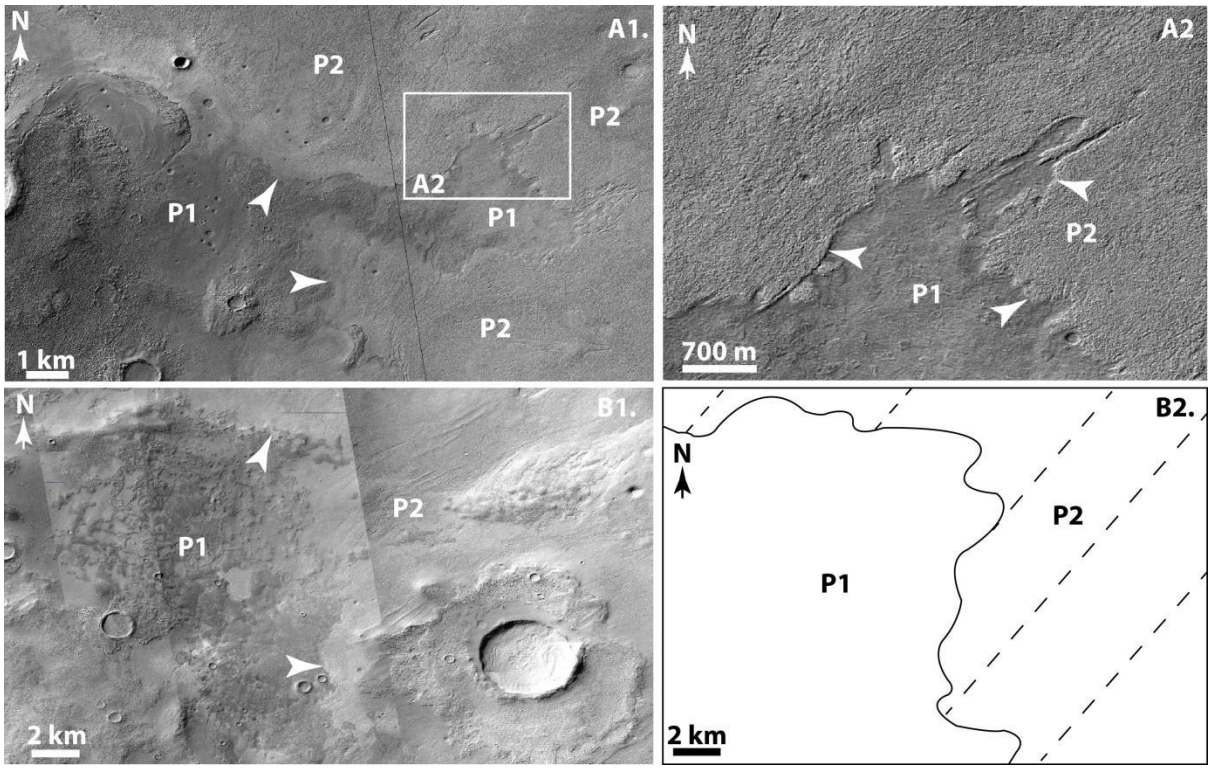

FIG10

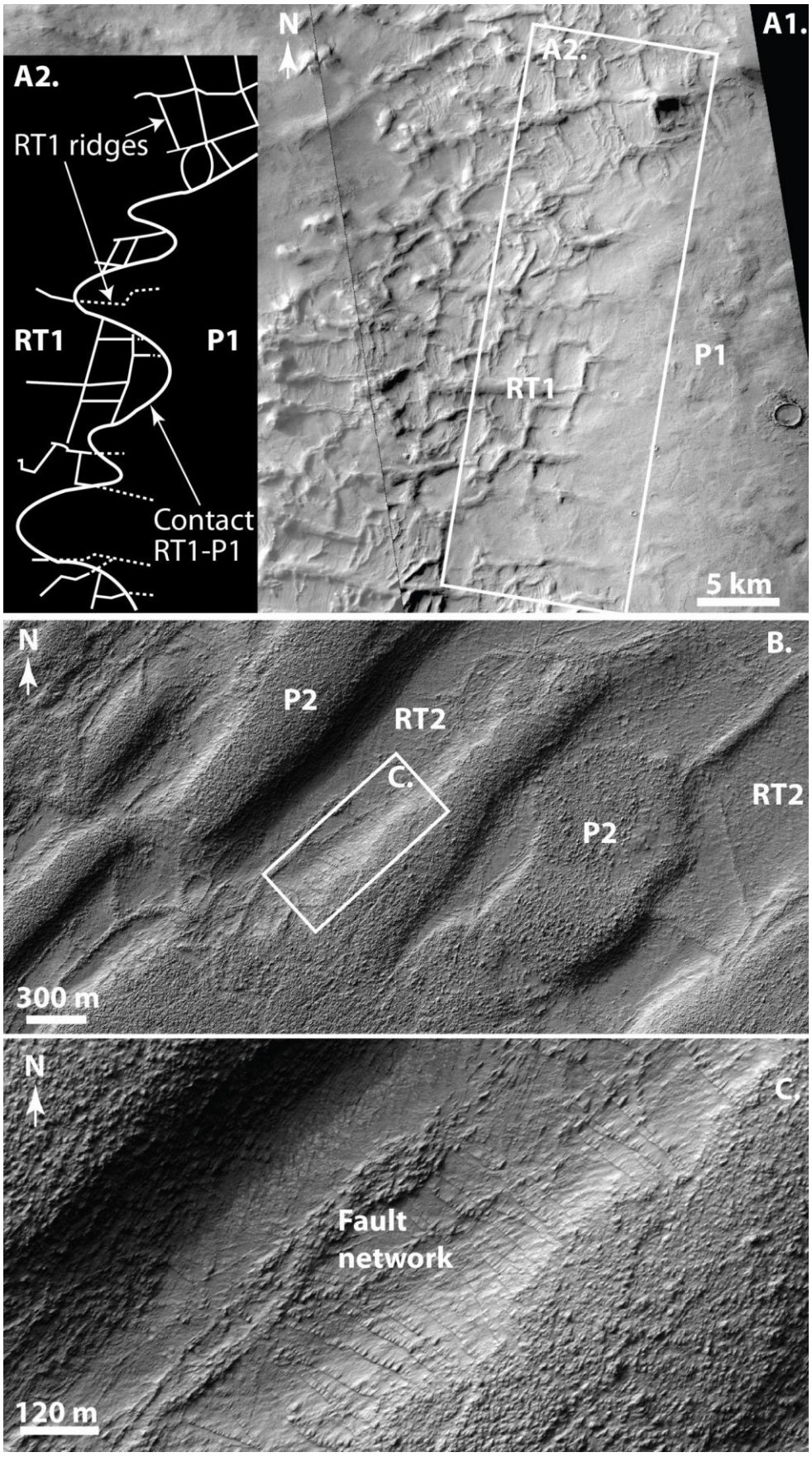
A2.
RT1 ridges
RT1
P1
Contact
RT1-P1
N
A1.
A2.
RT1
P1
5 km
N
B.
P2
RT2
C.
RT2
P2
300 m
N
C.
Fault
network
120 m

FIG11

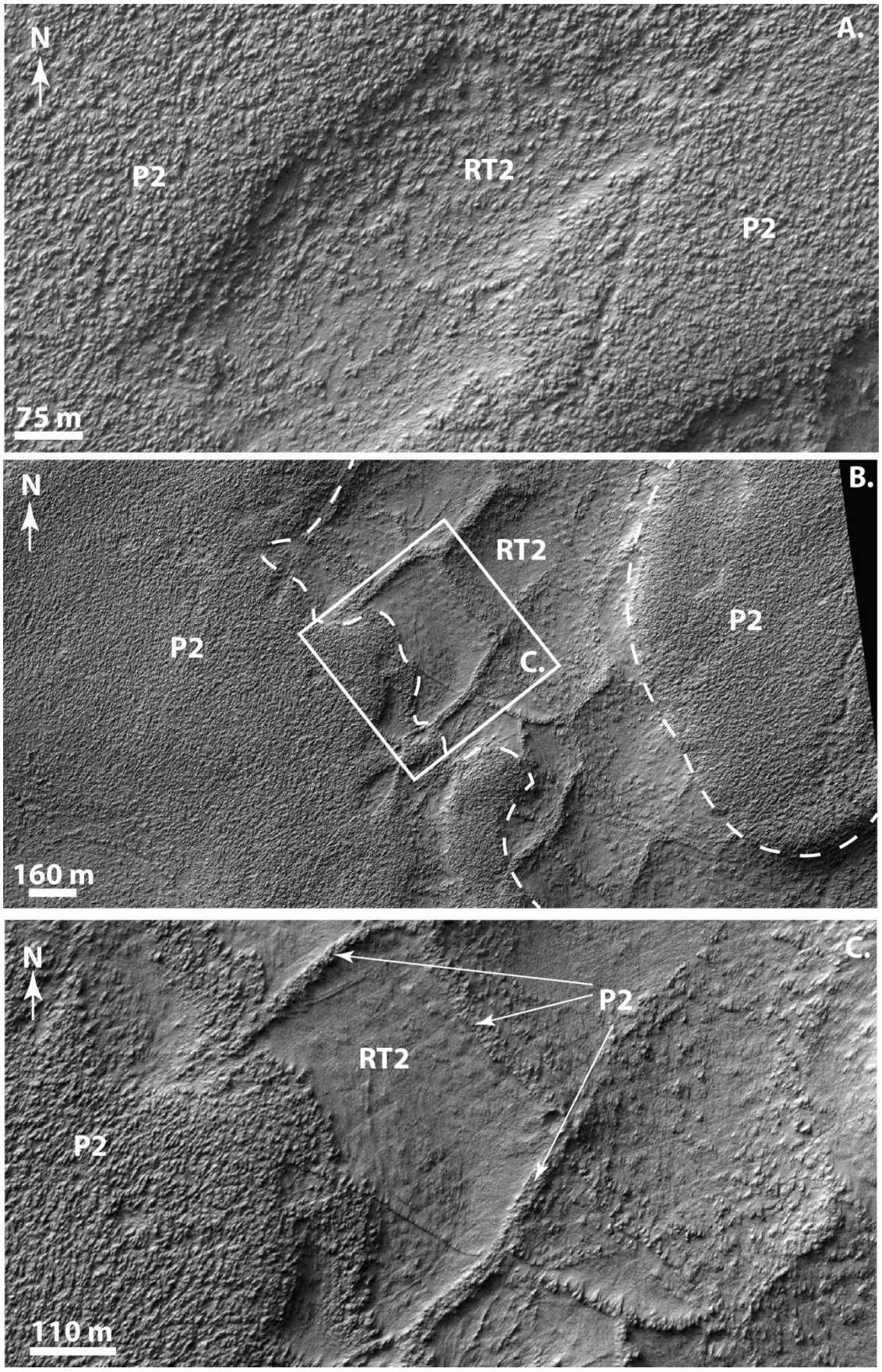

FIG12

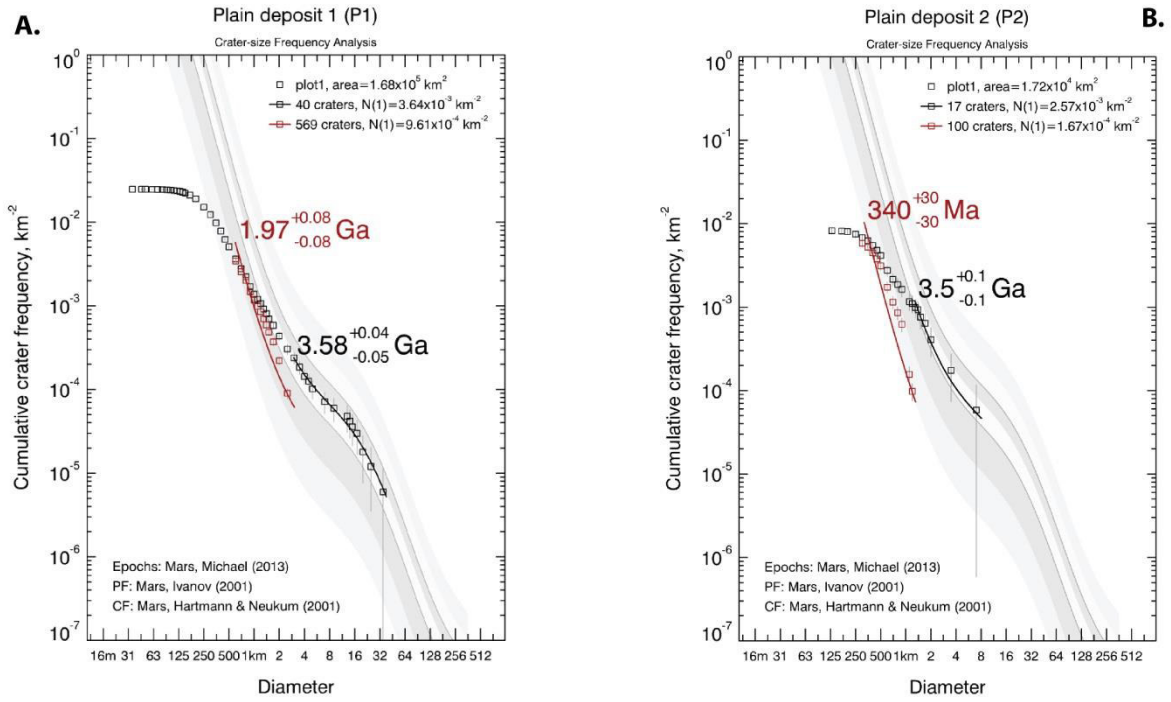
A.
Plain deposit 1 (P1)
Crater-size Frequency Analysis
plot1, area=1.68x10^5 km^2
40 craters, N(1)=3.64x10^-3 km^-2
569 craters, N(1)=9.61x10^-4 km^-2
1.97 +0.08 -0.08 Ga
3.58 +0.04 -0.05 Ga
Epochs: Mars, Michael (2013)
PF: Mars, Ivanov (2001)
CF: Mars, Hartmann & Neukum (2001)
Cumulative crater frequency, km^-2
16m 31 63 125 250 500 1km 2 4 8 16 32 64 128 256 512
Diameter
B.
Plain deposit 2 (P2)
Crater-size Frequency Analysis
plot1, area=1.72x10^4 km^2
17 craters, N(1)=2.57x10^-3 km^-2
100 craters, N(1)=1.67x10^-4 km^-2
340 +30 -30 Ma
3.5 +0.1 -0.1 Ga
Epochs: Mars, Michael (2013)
PF: Mars, Ivanov (2001)
CF: Mars, Hartmann & Neukum (2001)
Cumulative crater frequency, km^-2
16m 31 63 125 250 500 1km 2 4 8 16 32 64 128 256 512
Diameter

FIG13

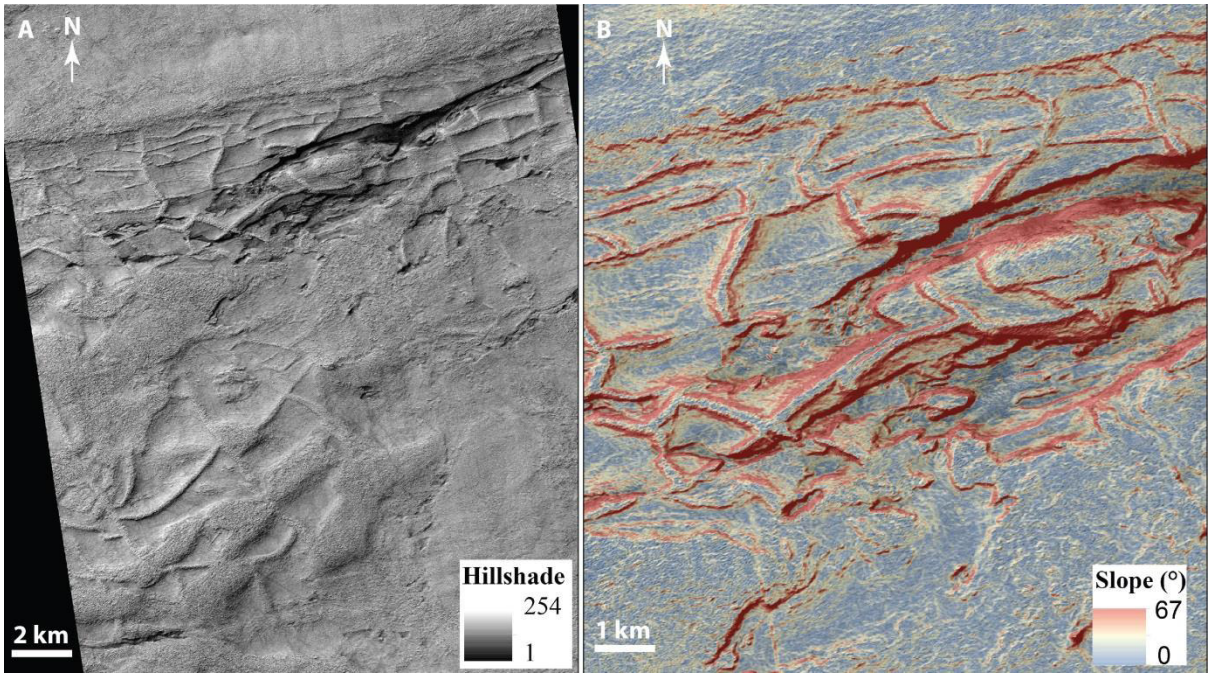
A
N
Hillshade
254
1
2 km
B
N
Slope (°)
67
0
1 km

FIG14

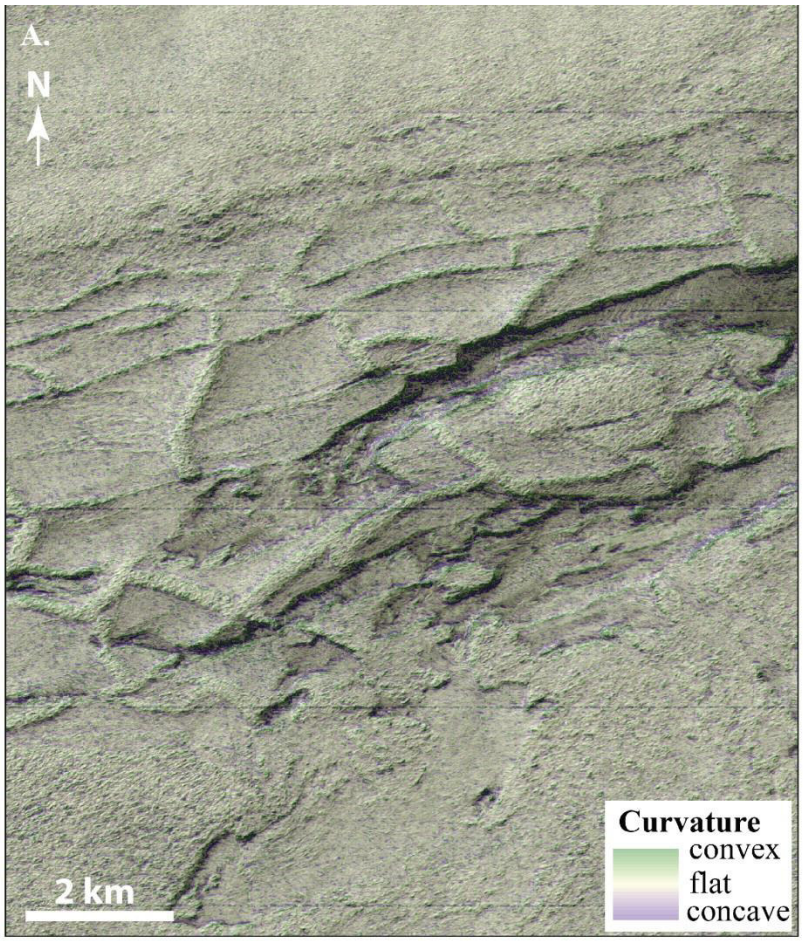
A.
N
2 km
Curvature
convex
flat
concave

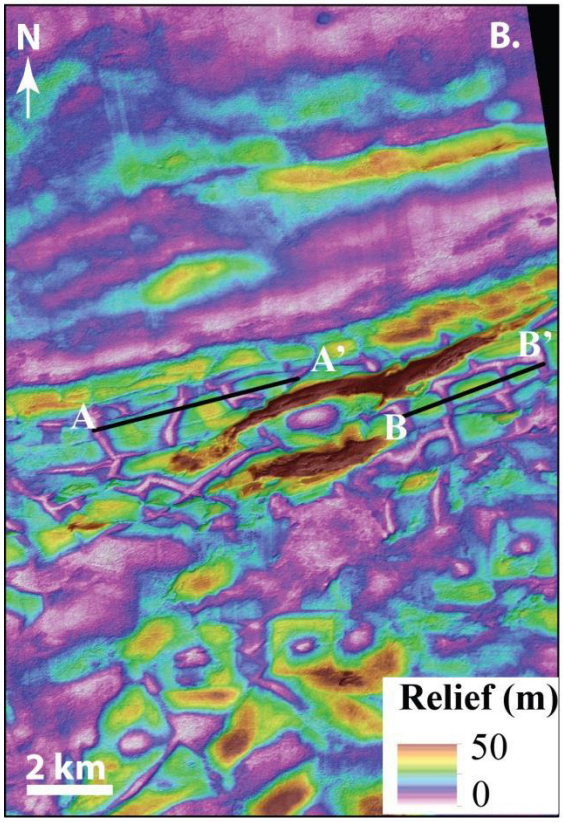
N
B.
A'
B'
A
B
2 km
Relief (m)
50
0

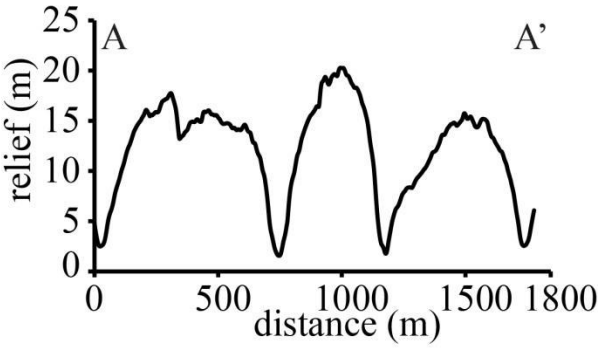
A
A'
relief (m)
25
20
15
10
5
0
0
500
1000
1500
1800
distance (m)

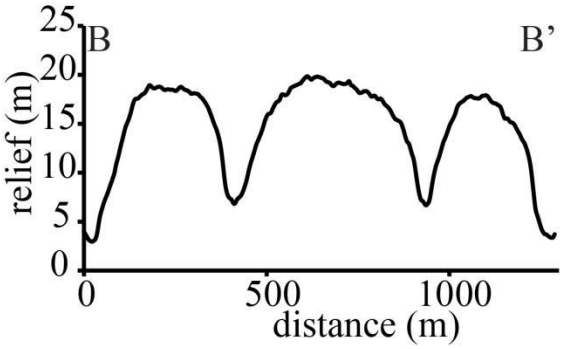
B
B'
relief (m)
25
20
15
10
5
0
0
500
1000
distance (m)

FIG15

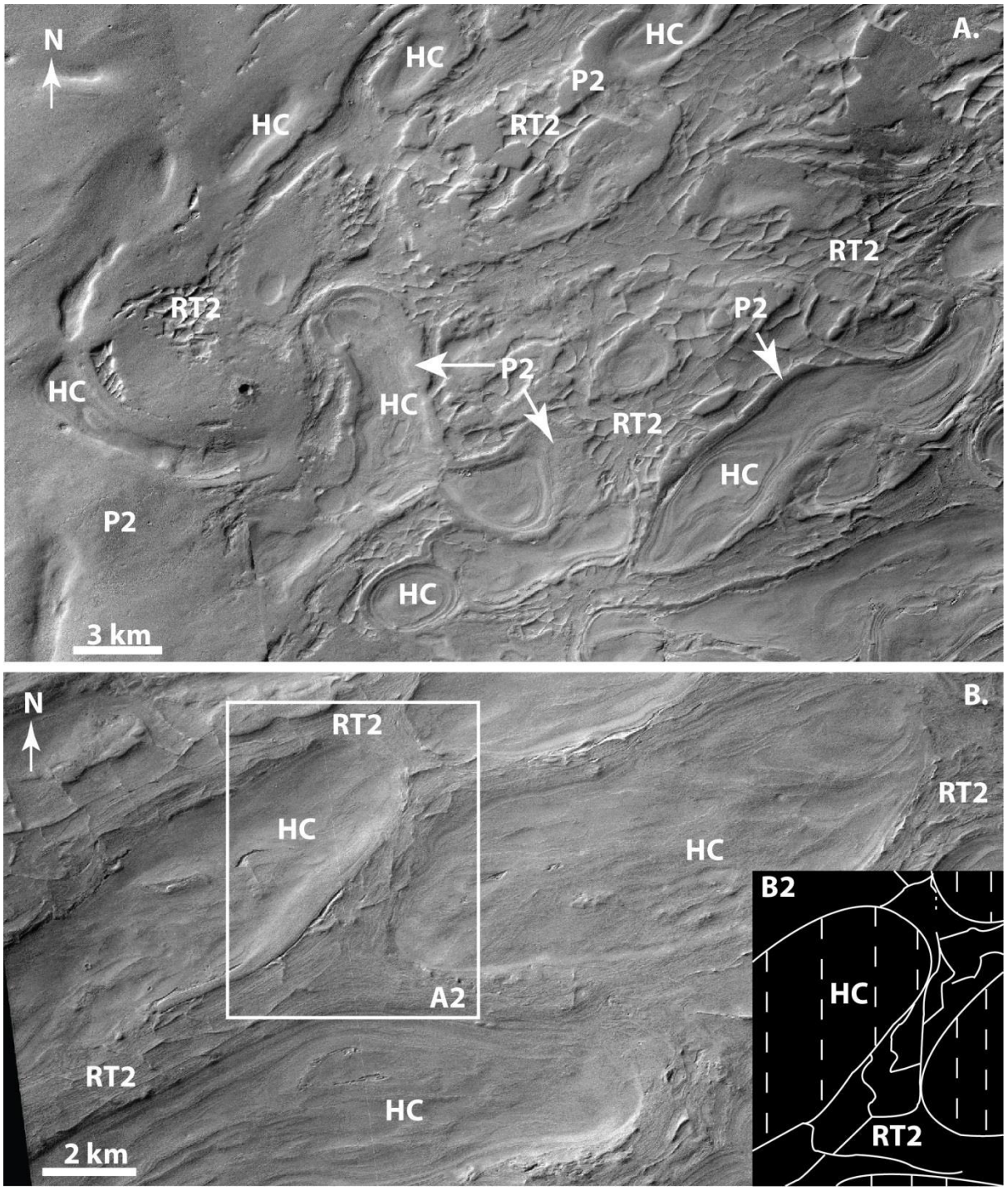
N
A.
HC
HC
HC
P2
RT2
RT2
RT2
P2
P2
HC
HC
RT2
HC
P2
HC
3 km
N
B.
RT2
HC
RT2
HC
A2
RT2
HC
B2
HC
RT2
2 km

FIG16

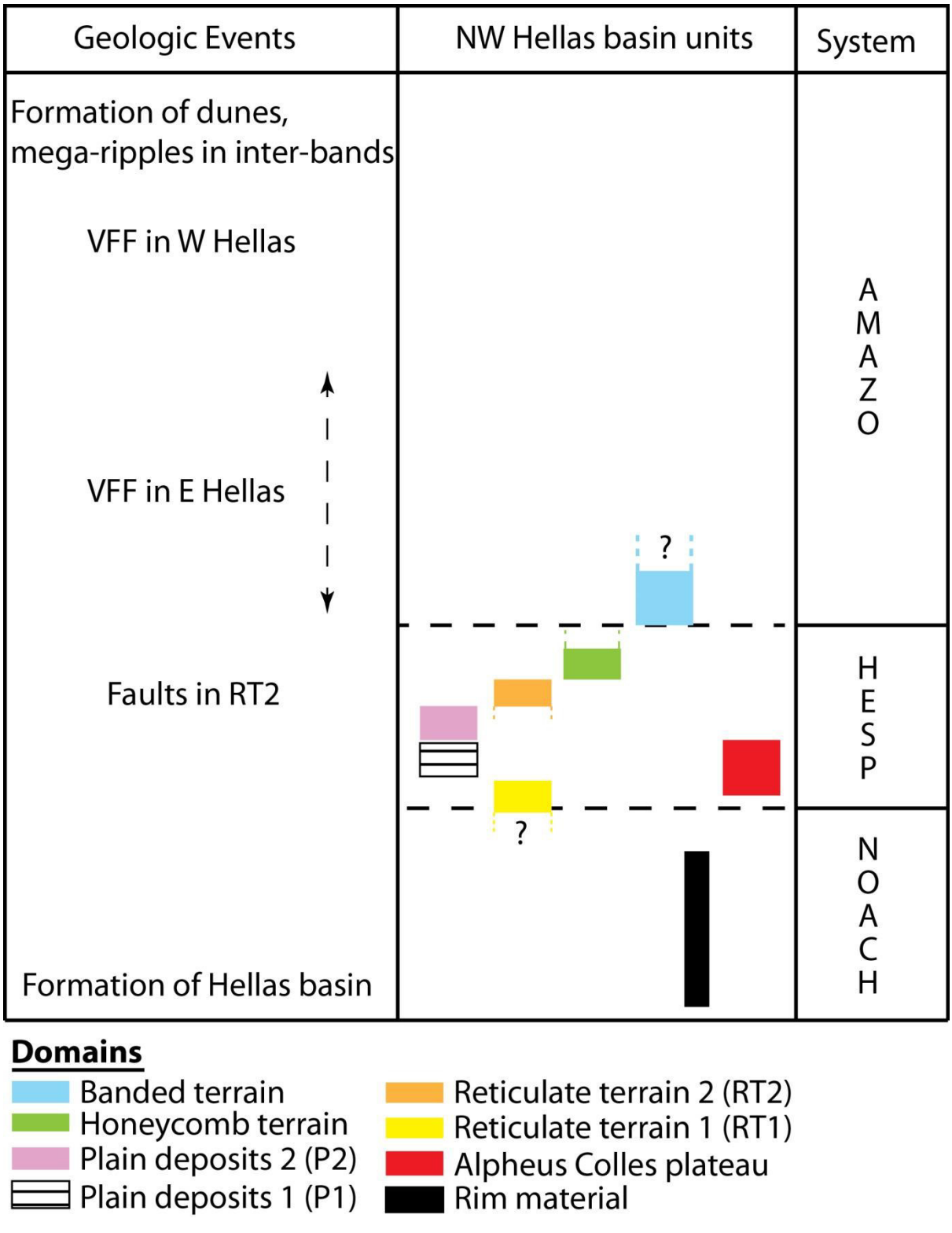
Geologic Events
NW Hellas basin units
System
Formation of dunes, mega-ripples in inter-bands
VFF in W Hellas
VFF in E Hellas
Faults in RT2
Formation of Hellas basin
?
?
AMAZO
HESP
NOACH
Domains
Banded terrain
Honeycomb terrain
Plain deposits 2 (P2)
Plain deposits 1 (P1)
Reticulate terrain 2 (RT2)
Reticulate terrain 1 (RT1)
Alpheus Colles plateau
Rim material

FIG17

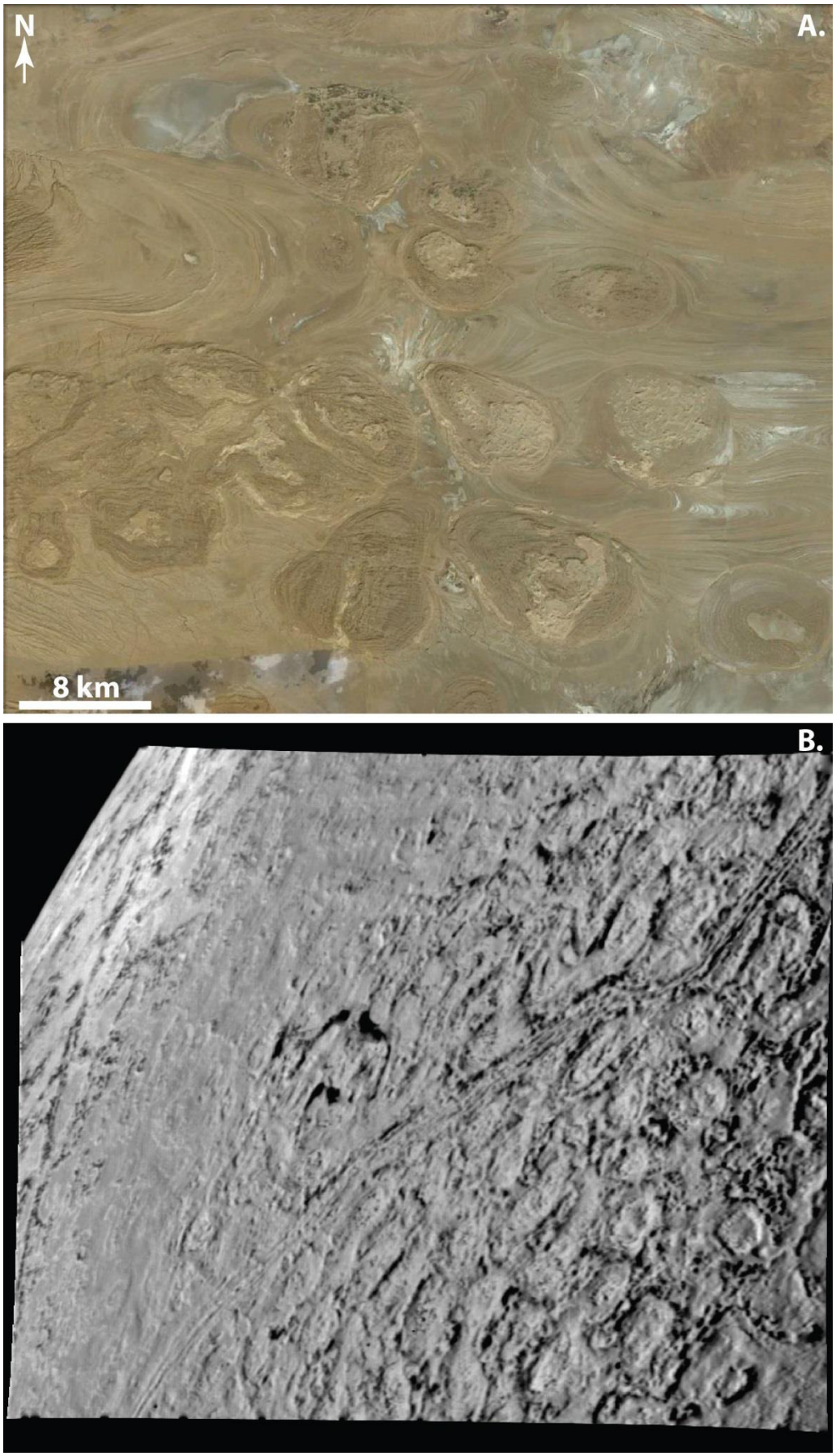

FIGS1

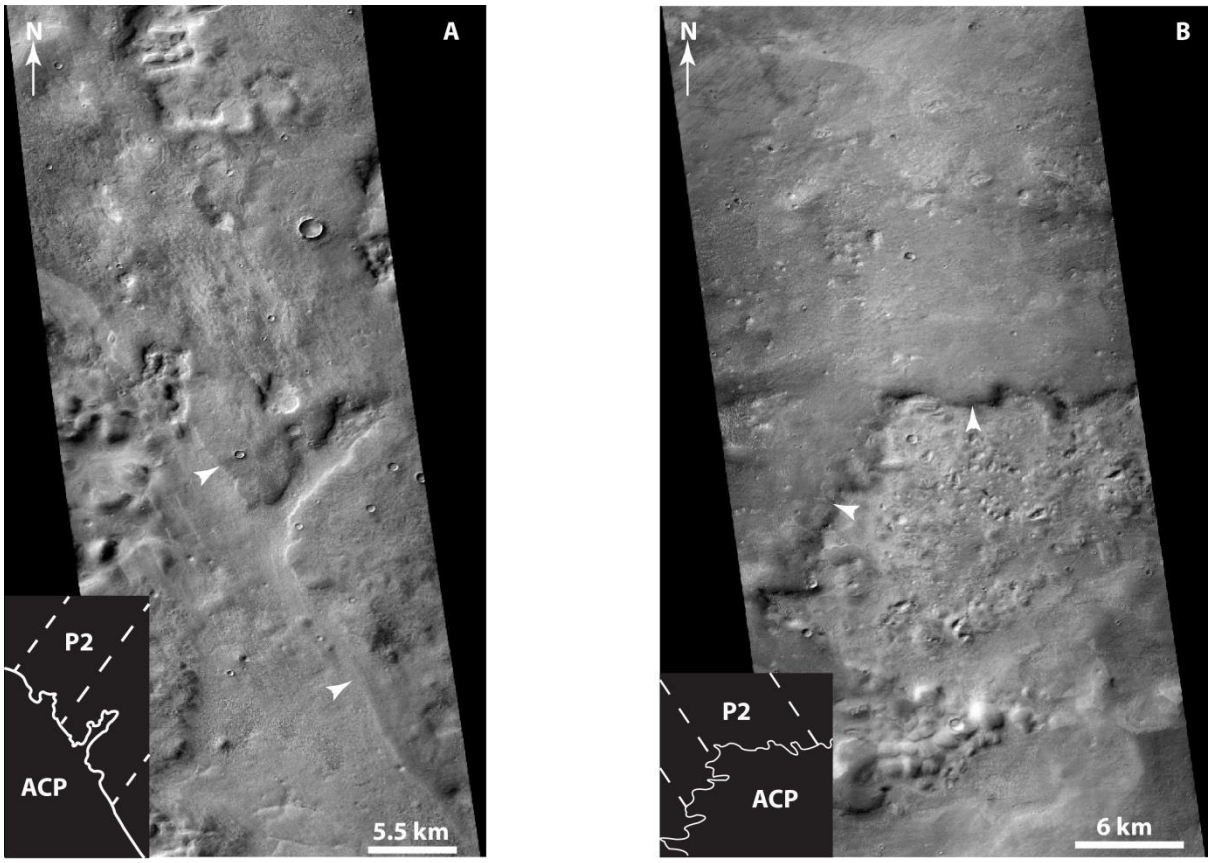

FIGS2

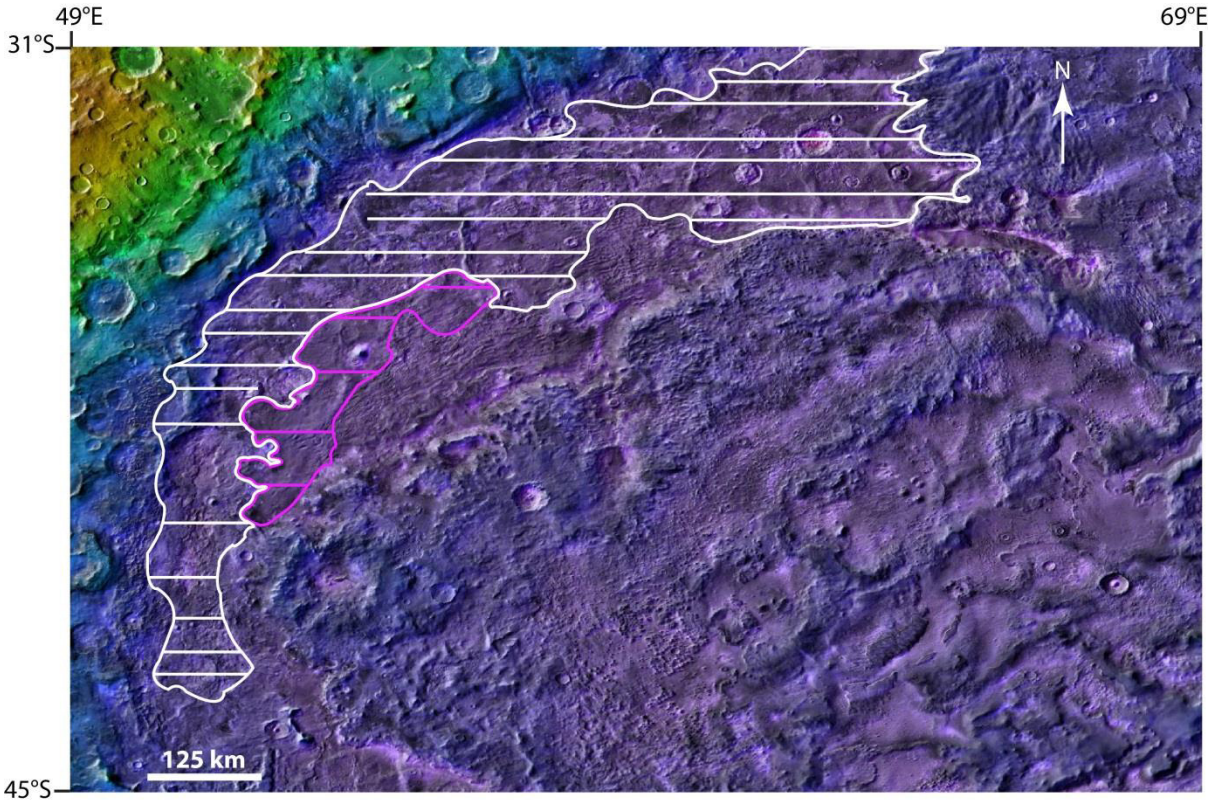

Domains	General morphology	Relative dating	Formations mechanism(s)
Alpheus Colles plateau (ACP) in the center Hellas.	➢ Large thick plateau. ➢ Belt of layered knobs in the NW part. Relatively smooth central part. ➢ Sinuous NW margin ➢ Fine-grained surface material (silt or fine sand).	➢ Overlapped in its eastern part by P2→ older than P2 ➢ Overlaid by some banded terrain → older than banded terrain	➢ Smooth central part could be due to a **remobilization of an ice-rich mantle** deposited during high-obliquity phases. ➢ NW Knobs belt could be due to the loss of ground ice
Banded terrain in the deepest part of Hellas.	➢ Alternation of sinuous bands and inter-bands ➢ Periglacial features on the surface. ➢ Fine–coarse partially cemented sand or silt.	➢ Youngest large deposition. ➢ Mostly connected to the NW ACP's margin. ➢ Locally located on the top of the ACP. ➢ Progressive transition with the honeycomb terrain.	➢ **Viscous flow of an ice-rich material** starting from the central ACP toward the north.
Two plain deposits (P1 and P2).	➢ P1: presence of local round-shaped knobs. ➢ P2: numerous angular pits on HiRISE images. ➢ P1 and P2:fine-grained material.	➢ P1 embayed by P2 → P1 older than P2 ➢ P2 overlaps the ACP in the east → P2 younger than the ACP	➢ **Deposition, erosion and remobilization of ice-rich mantle deposit.** ➢ Deposition of suspended material in a paleo-lake. ➢ Effusive low viscosity lava flows.
Two reticulate terrains: RT1 in the W Hellas, RT2 in the NW Hellas.	➢ Polygonal ridges separated by flat depression. ➢ RT1: depressions of 1–2 km across. ➢ RT2: depressions of 250–1,000 m across.	➢ RT1 overlaid by P1 → RT1 older than P1 and P2. ➢ RT2 enclosed in P2 → RT2 younger than P1 and younger or concurrent to P2.	➢ Periglacial degradation of P2.
Honeycomb terrain.	➢ Cells: depressions with ridges more or less distinct. ➢ Cemented sand-sized material.	➢ Enclosed in P2. ➢ Cells deformed RT2 ridges → post-dates RT2. ➢ Some cells contains banded terrain → older than banded terrain	➢ Ice diapirism: extrusion of over-pressured ice buried below the surface. ➢ Magmatic diapirism. ➢ Salt diapirism.